ROYAL SOCIETY OF CHEMISTRY

ARTICLE

An outstanding effect of graphite in nano-MgH₂-TiH₂ on hydrogen storage performance†

Mykhaylo Lotoskyy*[a], Roman Denys [b], Volodymyr A.Yartys*[c], Jon Eriksen [b], Jonathan Goh [a], Serge Nyallang Nyamsi [a], Cordellia Sita [a] and Franscious Cummings [d]

TiH₂–modified MgH₂ prepared by high energy reactive ball milling (HRBM) of Mg and Ti in hydrogen shows high weight H storage capacity and fast hydrogenation / dehydrogenation kinetics. However, decrease of the reversible H storage capacity on cycling at high temperatures takes place and is a major obstacle for their use in hydrogen and heat storage applications. Reversible hydrogen absorption / desorption cycling of the materials requires use of the working temperature ≥350 °C and results in a partial step-by-step loss of the recoverable hydrogen storage capacity, without significant changes in the rates of hydrogenation / dehydrogenation. After hydrogen desorption at 330–350 °C, hydrogen absorption can proceed at much lower temperatures, down to 24 °C. However, a significant decay of the hreversible hydrogen capacity takes place with increasing number of cycles. The observed deterioration is caused by cycling-induced drastic morphological changes in the studied composite material leading to segregation of TiH₂ particles in the cycled samples instead of their initial homogeneous distribution. However, introduction of 5 wt.% of graphite into the MgH₂ – TiH₂ composite system prepared by HRBM leads to an outstanding improvement of the hydrogen storage performance. Indeed, hydrogen absorption and desorption characteristics remain stable through the 100 hydrogen absorption / desorption cycles caused by an effect of the added graphite. TEM study showed that carbon is uniformly distributed between the MgH₂ grains covering segregated TiH₂, preventing their growth and thus keeping unchanged the reversible storage capacity and rates of hydrogen charge and discharge. Modelling of the kinetics of hydrogen absorption and desorption in the Mg–Ti and Mg–Ti–C composites showed that the reaction mechanisms significantly change depending on a number of parameters including; presence or absence of graphite, number of absorption-desorption cycle and H absorption temperature.

1. Introduction

Magnesium hydride, MgH₂ (7.66 wt.% H / ~110 kg H/m³), is a promising material for weight efficient hydrogen storage applications operating at moderately high, ≥300 °C, temperatures [1-4]. Further to hydrogen storage, MgH₂ and Mg-based hydrides are utilised in heat storage with working temperatures T=250–550 °C [5-7]. At the same time, slow hydrogenation / dehydrogenation kinetics and decrease of H storage capacity on cycling at high temperatures are the major obstacles for the applications utilising MgH₂. Necessity to address this challenge stimulated a great interest worldwide to magnesium-based hydrogen storage materials which continues for more than four decades. Analysis of the reference literature on the metal – hydrogen systems published since 2010 (see, e.g., materials of the International Symposia MH2010–2016 [8-11]) shows that 20–25% of the works on the topic deal with the hydrogen storage materials based on magnesium and magnesium alloys.

In the recent years, the reactive ball milling (RBM) in inert or hydrogen atmosphere, of the mixture of Mg/MgH₂ with additives/catalysts, has been in focus as a method of the synthesis of magnesium-based nanostructured materials with improved hydrogen storage performance. A variety of additives has been used during the RBM to improve H sorption / desorption kinetics including; 3d-transition metals and alloys [12-26], metal oxides [15,27-32], hydrides (TiH₂ [24-26,33-38] or ZrH₂ [39]), carbon materials [23,40-55], and halides of transition metals [56,57]. Hydrogen storage performances of various types of Mg-based nanostructured hydrogen storage materials were reviewed in Refs [2,3,58,59]; a brief summary of the selected data for some materials is presented in Table 1. Hydrogen storage materials based on MgH₂–TiH₂ nanocomposites keep advantages offered by individual MgH₂ for their use in hydrogen storage applications allowing gravimetric efficiency of hydrogen storage of 4–6 wt% H and in

a. HySA Systems Competence Centre, South African Institute for Advanced Materials Chemistry, University of the Western Cape, Private Bag X17, Bellville 7535, South Africa, mlototskyy@uwc.ac.za
b. HYSTORSYS AS, P.O. Box 45, Kjeller NO-2027, Norway, roman.denys@hystorsys.no
c. Institute for Energy Technology, P.O. Box 40, Kjeller NO-2027, Norway, volodymyr.yartys@ife.no
d. Electron Microscope Unit, University of the Western Cape, Robert Sobukwe Road, Bellville 7535, South Africa, fcummings@uwc.ac.za
† Electronic Supplementary Information (ESI) available [file Mg_Ti-Suppl.pdf]: See DOI: 10.1039/x0xx00000x

This journal is © The Royal Society of Chemistry 20xx

J. Mater. Chem. A, 2018, 00, 1-3 | 1

An outstanding effect of graphite in nano-MgH$_2$-TiH$_2$ …   **Journal of Materials Chemistry A**

applications allowing storage of a medium-grade heat at a temperature potential of T=350–450 °C. Mg–Ti composites are characterised by exceptionally fast hydrogen absorption / desorption kinetics due to the catalytic effect of titanium species facilitating processes of hydrogen absorption and desorption. Such enhanced kinetics is similar to the performance of the MgH$_2$ + Nb$_2$O$_5$ nanocomposites, one of the best Mg-based hydrogen storage materials known to date [24]. Relatively close values of decomposition temperatures of MgH$_2$ (up to 400 °C) and TiH$_2$ (~550 °C) [60], would allow efficient use of the Mg–Ti–H system for both hydrogen storage and efficient thermal management in energy systems utilising reversible solid oxide fuel cells (R-SOFC) with a temperature potential of the dissipated heat around 600 °C [61,62]. However, a major issue is in a poor stability of hydrogen sorption performance of MgH$_2$–TiH$_2$ nanomaterials during their cyclic dehydrogenation / re-hydrogenation at the higher temperatures, including drop of the reversible hydrogen storage capacity and gradual deterioration of hydrogen absorption / desorption kinetics.

Table 1. Selected data on hydrogen storage materials on the basis of nanostructured/catalysed MgH$_2$.

Additive		Main component; RBM atmosphere (P [bar]), duration [hours], BPR	Hydrogen storage performance			Ref
Group	Specification		Dehydrogenation	Re-hydrogenation	Capacity drop during cycling	
No additives	–	MgH$_2$; no RBM	5-6 wt% H in 30 min (1.5 bar / 380 °C)	6 wt% H in 60 min (23 bar / 360 °C)	25% / 150 cycles	[1]
		Mg; H$_2$ (30), 6, 40:1	7 wt%H (vacuum / 320-415 °C)	4.5 wt% H in 120 min (15 bar / 250 °C)	6% / 10 cycles	[52]
Metals and alloys	Ni (5 mol%)	MgH$_2$; Ar (1), 20, 10:1	5 wt%H in 6 min (0.15 bar / 300 °C)	5 wt% H in 20 min (10 bar / 200 °C)	0 / >3 cycles	[2,13]
	Pd (1 wt%)	Mg; Ar (1), 20, 30:1[a]	5 wt%H in 30 min (1 bar / 330 °C)	5 wt% H in 60 min (10 bar / 230 °C)	No data	[12]
	BCC-V–Ti–Zr–Cr alloy (10 wt%)	Mg; H$_2$ (30), 2, 80:1	5 wt%H (vacuum / 200-250 °C)	5 wt% H in 10 seconds (26 bar / ≥100 °C)	0 / 4 cycles[b]	[19]
	V (5 mol%)	MgH$_2$, Ar (1), 20, no data	5.5 wt% H in 12 min (0.25 bar / 300 °C)	5.5 wt% H in 5 min (10 bar / 300 °C)	0 / 2000 cycles[b,c]	[14]
	BCC-V–Ti–Cr alloy (5 mol%)	MgH$_2$; H$_2$ (150), 4, 10:1	5 wt%H in 5 min (0.1 bar / 300 °C)	5.5 wt% H in 15 min (4 bar / 300 °C)	27% / 51 cycle	[25]
Hydrides	TiH$_2$ (5 mol%)	MgH$_2$; H$_2$ (150), 4, 10:1	4.2 wt%H in 5 min (0.1 bar / 300 °C)	4.5 wt% H in 15 min (4 bar / 300 °C)	17% / 51 cycle	[25]
	TiH$_2$ (10 mol%)	MgH$_2$; H$_2$ (138), 4, 35:1	6 wt%H in 15 min (0.01 bar / 300 °C)	6 wt% H in 60 min (20 bar / 300 °C)	5% / 80 cycles[b]	[34]
Oxides	Nb$_2$O$_5$ (0.5 mol%)	MgH$_2$; Ar (1), 120, 10:1	7 wt%H in 1.5 min (vacuum / 300 °C)	6 wt% H in 1 min (8.4 bar / 250 °C)	No data	[27]
	FeTiO$_3$ (10 wt%)	Mg; H$_2$ (30), 1, 40:1	6 wt%H (vacuum / 250-350 °C)	2.7 wt% H in 30 min (15 bar / 250 °C)[d]	No data	[31]
Carbon[e]	G, AC, MWCNT, TEG (≤5 wt%)	Mg; H$_2$ (30), 2, 40:1	7 wt%H (vacuum / 280-460 °C)	5 wt% H in 60 min (15 bar / 250 °C)	0 / 10 cycles	[52]

Notes: [a] grain size 30 nm; [b] deterioration of H desorption kinetics; [c] ~1.5x increase of the crystallite size; [d] 5–5.5 wt% H at the same conditions when 5 wt% of carbon (AC, MWCNT, G)[e] was additionally introduced; [e] G – graphite, AC – activated carbon, MWCNT – multi-wall carbon nanotubes, TEG – thermally expanded graphite.

Amirkhiz et al. [21] performed sorption cycling tests of MgH$_2$ ball milled in argon with 10% Ti and 10% FeTi. Despite fast desorption kinetics after about 5 activation cycles, the kinetics degraded throughout further cycling, eventually slowing down by a factor of 7 and 4, respectively. Important, that a uniform dispersion of the Ti (TiFe) catalyst on the surface of MgH$_2$ particles and, in turn, good dehydrogenation kinetics and better cycling stability were achieved by the addition of minor amount of carbon (2.5 wt% of multi-wall carbon nanotubes) to the mixture prior to the ball milling.

Zhou et al. [25,26] systematically investigated the cyclic stability of the kinetics of MgH$_2$ prepared by high energy ball milling in H$_2$ catalysed by TiH$_2$, TiMn$_2$ and VTiCr. The results showed that the kinetics of high-temperature (300 °C) hydrogenation and dehydrogenation maintained a good stability during 100 hydrogen absorption/desorption cycles. However, there was a degradation in hydrogen capacities; a loss of 0.4 wt%, 0.2 wt% and 1.0 wt % for the TiH$_2$, TiMn$_2$ and VTiCr catalysts, respectively, was observed. When testing the hydrogenation kinetics in the low-temperature range (25 to 150 °C), a severe degradation was observed after the cycling. XRD analysis showed the increase of Mg and MgH$_2$ crystallite size during the cycling. The catalysts grains size increased with a change of their distribution in the cycled material compared to the as-milled one.

Kalisvaart et al. [63] focused their investigation on 1.5 μm thick Mg-based films with Al, Fe and Ti as alloying elements. The Mg–Ti system (atomic ratio Mg$_{75}$Ti$_{25}$) showed a severe degradation in hydrogen sorption performance with a drop of

reversible H capacity from 5.2 wt% to 3.6 wt% throughout 25 hydrogenation/dehydrogenation cycles at T=200 °C.

We note that most of published studies of cycling stability of MgH_2-based nanocomposites were carried out at the maximum operating temperature not exceeding 300 °C (see Table 1). At the same time, further increase of the operating temperature (the range 350–450 °C is the most interesting from the application point of view) results in dramatic deterioration of hydrogen sorption performance already at first hydrogen absorption / desorption cycles [52].

During the last 10-15 years, significant attention was paid to hydrogen storage materials on the basis of Mg prepared by RBM with additives of various carbon species: graphite [23,31,40,41,43,47,48,51,52], activated carbon [31,43,49, 50,52], carbon nanotubes [31,43,45,46,48,52] and nanofibres [23,43], soot [44,48], expanded natural graphite [52], demineralised anthracite coal [42,53,54], nanodiamonds [44,48]. The introduction of the carbon additives was shown to result in the improvement of hydrogen sorption / desorption performance including significant increase of its stability during H absorption-desorption cycling at high temperatures. This effect was associated with the distribution of carbon in between nanoparticles of $Mg(H_2)$ during RBM preventing their coalescence and surface oxidation [47,48,54].

In our earlier publication [52], we proposed that the effect of sp^2-hybridized carbon additives to Mg has roots in their destruction during the RBM in H_2 to form graphene layers encapsulating the MgH_2 nanoparticles and preventing the grain growth. It results in an increase of absorption–desorption cycle stability and a decrease of the MgH_2 crystallite size in the re-hydrogenated Mg–C materials as compared to Mg alone. Recent study of composite materials prepared by a synthesis of MgH_2 nanoparticles on graphene nanosheets [55] and exhibiting improved and stable dehydrogenation kinetics indirectly confirmed our assumption. A direct experimental evidence of significant improvement of hydrogenation / dehydrogenation kinetics in H_2–Mg system by adding graphene nanoplatelets (GNP) was recently published by Ruse et al. [64].

It has to be noted that kinetic improvements in the formation / decomposition of MgH_2 in the carbon-containing materials on its basis were found to be more pronounced when minor amounts (≤5-10 wt%) of the carbon additives were introduced together with catalytic additives of transition metals or oxides [23,31,32,43,46,50,65]. This synergetic effect was explained by the facilitation of hydrogen dissociation / recombination on the surface of the catalyst while the carbon species played the role of efficient mediator of the H atoms between the catalyst and $Mg(H_2)$ [44,50]. In addition, carbon may also inhibit oxidation of $Mg(H_2)$ with oxide additives during cyclic H absorption / desorption and thus to avoid the deterioration of reversible hydrogen storage capacity of the material [31].

Summarising a brief review presented above, we can conclude that, due to intensive studies undertaken during the last two decades, there has been developed a number of promising hydrogen storage materials on the basis of catalysed nanostructured MgH_2, preferably, prepared using RBM methods. Special attention has been paid to MgH_2–TiH_2

materials characterised by reversible storage capacity up to 6 wt.% H and fast H_2 absorption / desorption kinetics. However, stability of H sorption performance and cycle life at high operating temperatures (particularly, deterioration of low-temperature hydrogen absorption kinetics after dehydrogenation at T>300 °C) still remain a challenge.

From the other hand, introduction of carbon additives to Mg taken alone or with additives of metallic or oxide catalysts results in the significant improvement of reversible H capacity and cycle stability of the Mg-based hydrogen storage materials. It is expected that similar effect will be observed for the hydride-catalysed materials, particularly, MgH_2–TiH_2–C prepared by RBM of Mg, Ti and carbon in hydrogen atmosphere. Identification of the compositions and preparation routes for the materials of practical interest requires in-depth study of the interrelation between these process parameters, phase and morphological changes in the materials during their prolonged hydrogenation / dehydrogenation cycling, as well as evolution of the hydrogen absorption / desorption properties.

In the present work, we report about experimental study of phase and elemental composition, morphology, hydrogen absorption / desorption performance (including kinetics) and cycling stability of Mg–Ti nanostructured hydrogen storage materials prepared from the elemental metal powders with and without carbon additives, by high-energy reactive ball milling in H_2.

2. EXPERIMENTAL

2.1. Preparation of the samples.

MgH_2–TiH_2 hydrogen storage materials have been prepared by high energy reactive ball milling of pure metals under hydrogen gas (HRBM). Mg grit (−20 +100 mesh, purity >99 %) and Ti powder (150 mesh, purity >99.9 %) were used as starting materials. The amounts of Mg and Ti taken for the preparation of the samples corresponded to the formulae $Mg_{0.5}Ti_{0.5}$, $Mg_{0.75}Ti_{0.25}$, and $Mg_{0.9}Ti_{0.1}$ further referred in the text. For the latter composition, a carbon-containing sample was also prepared, by the addition of 5 wt.% of graphite powder (≤20 μm, purity >99%) to the initial Mg + Ti mixture; this sample will be further referred as $Mg_{0.9}Ti_{0.1}$ + 5% C.

The milling was carried out in a custom-built 80 mL Duplex SS2377 vial using Fritsch P6 planetary mill. The balls-to-powder ratio was 40:1 (sample weight 3.2 g; 30 steel balls, 10 mm in the diameter). The milling was performed at a rotation speed of 500 rpm. The vial was initially evacuated under high vacuum and filled with hydrogen gas (purity 99.999%) at a pressure of 20 bar. To monitor the hydrogenation process, the milling was paused (typically in 15–30 min intervals) and the vial, after cooling to room temperature, was connected to a Sieverts-type apparatus to check the amount of hydrogen absorbed; the vial was then refilled to reach 20 bar H_2, and the milling was continued. Total milling time for each sample was 240 to 390 min.

For the comparison purposes, the samples on the basis of individual Mg (further referred as Mg) and Mg with the additive of 5 wt.% the graphite powder ([52]; further referred as Mg + 5% C) have been prepared at the same conditions.

2.2. Hydrogen absorption and desorption studies.

Hydrogen desorption from the as-prepared samples was studied by Thermal Desorption Spectroscopy (TDS). 300–500 mg of the sample was loaded into a reactor which, together with the measurement system, was evacuated at the room temperature to <10^{-4} mbar. The TDS measurements were performed by heating the reactor at a constant heating rate of 2 K min^{-1} from room temperature to 600 °C under dynamic vacuum conditions, when H$_2$ desorption results in the pressure increase in the evacuation system. The vacuum sensor was calibrated by using a known flow rate of H$_2$ gas into the system.

TDS measurements were also performed for the re-hydrogenated samples[*], by their heating from room temperature to 350 °C at constant heating rates in the range 0.5–8 K min^{-1} under the dynamic vacuum conditions. During the TDS experiments the weight of the samples (110–295 mg) was taken to provide approximately equal MgH$_2$ content; so during the heating they would release about the same amount of H$_2$ providing the same thermal effect. In all cases the re-hydrogenation was carried out at T=300 °C and P=20 bar.

The TDS data was further processed by Kissinger method [66,67] to yield apparent activation energy, E$_A$, for hydrogen desorption using the following equation:

$$\ln\left(\frac{\beta}{T_m^2}\right) = \ln\left(\frac{Z\,R}{E_a}\right) - \frac{E_A}{R\,T_m}; \tag{1}$$

where β [K min^{-1}] is a heating rate, T_m [K] is a peak temperature, R=8.3143 J mol^{-1} K^{-1} is a universal gas constant, Z [min^{-1}] and E_A [J mol^{-1}] are, respectively, pre-exponent and activation energy of Arhenius equation determining temperature dependence of the rate constant, k(T):

$$k(T) = Z\,exp\left(-\frac{E_A}{R\,T}\right). \tag{2}$$

The value of $\frac{E_A}{R}$ was determined from a slope of a Kissinger plot of $y = \ln\left(\frac{\beta}{T_m^2}\right)$ versus $x = \frac{1}{T_m}$, similarly to the procedure used in studies of dehydrogenation performance of nanocrystalline MgH$_2$ (see, e.g. [68]).

The changes of dehydrogenation mechanism during H$_2$ absorption / desorption cycling retrieved from the TDS data were evaluated by their modelling using a procedure recently developed by the authors [69]. The model uses a combination of modified Kissinger approach and combined form of differential kinetic equation:

$$r \equiv \frac{dX}{dt}(T,X) = Z\,exp\left(-\frac{E_A}{R\cdot T}\right) \cdot f(X)\,; \tag{3}$$

where r is the reaction rate, X is the reacted fraction, and $f(X)$ is the rate dependence function related to the reaction mechanism (reaction model). Other multiplier in the right-hand part of Eq. 3 is a rate constant assumed to follow the Arrhenius law (Eq. 2). The function $f(X)$ was modelled according to Šesták and Berggren [70]:

$$f(X) = X^M \cdot (1-X)^N \cdot [-ln(1-X)]^P; \tag{4}$$

where various combinations of the values of model parameters M, N and P correspond to the various reaction controlling mechanisms.

The modelling procedure [69] allows to visualise dependence of the ratio $f(X)/f(X_m)$ on the reactied fraction, X, experimentally determined from the TDS data. Here X_m is a value of the reacted fraction which corresponds to the peak maximum observed at a temperature T_m, and the model parameters (Z, E_A, M, N, P) are obtained by the data fitting which included (i) starting estimation of Z and E_A from a modified Kissinger plot ($r(X_m)$ versus T_m); (ii) refinement of the whole TDS dataset at starting values M=1, N=2, P=0; and (iii) individual refinements of separate spectra at the starting values of the fitting parameters obtained on the step (ii). More details about the modelling and refinement procedure are presented in ref. [69].

The experiments on kinetic cycle stability of the materials during the hydrogen absorption / desorption (up to 105 cycles) were carried using the same Sieverts apparatus. Hydrogen absorption was performed for 30 min at T=350 °C and initial H$_2$ pressure of 10 bar (final H$_2$ pressure about 8.5 bar), and desorption was performed for 10 min at T=350 °C and starting pressure of 1.5 bar (final H$_2$ pressure about 3 bar)[§]. Kinetic studies of the samples Mg$_{0.9}$Ti$_{0.1}$ (5 cycles) and Mg$_{0.9}$Ti$_{0.1}$+5% C (50 cycles) also included the measurements of H$_2$ absorption kinetics at the lower temperatures (25–330 °C) followed by H$_2$ desorption at T=280–330 °C; more details are presented in *Supplementary Information, Table S1*.

The data acquisition interval was equal to 5 s for the TDS experiments, and 1 s during studying cycle stability and kinetic measurements.

The collected datasets for hydrogen absorption during HRBM and hydrogen desorption in the course of cycle stability studies were used in analysis of the formal kinetics of the processes performed using Avrami-Erofeev equation[#]:

$$X = N/N_{max} = 1 - exp[-(kt)^n]; \tag{5}$$

where X=0...1 is the actual value of the reacted fraction, t is time, k is the rate constant, and n is an exponential factor indirectly related to the reaction mechanism. The reacted fraction was determined as X=N/N_{max} where N and N_{max} correspond to the actual and maximum values, respectively, of the amount of H$_2$ absorbed in or desorbed from the sample.

Better fit of the kinetic data collected for hydrogen absorption in the course of cycle stability studies was obtained assuming that the hydrogenation is contributed by two processes, fast (1) and slow (2). The resulting kinetics was approximated by the following modification of the Avraami-Erofeev equation:

$$N = A_1\{1 - exp[-(k_1 t)^{n_1}]\} + A_2\{1 - exp[-(k_2 t)^{n_2}]\}; \tag{6}$$

where the rate constant k_1>k_2, and A_1, A_2 are the contributions of the processes 1 and 2, respectively, in the amount of hydrogen, N, absorbed in the sample. In doing so, the fraction, w_i, of the each stage can be calculated as w_i=A_i/N_{max}.

2.3. Phase composition and morphology.

The XRD studies were performed using Bruker AXS D8 Advance instrument, Cu-Kα radiation, λ_1 = 1.5406 Å, λ_2 = 1.5444 Å, λ_2/λ_1 = 0.5. The Bragg angle range was 2θ = 20–90° with a scanning step of 0.0275°. A standard α-Al$_2$O$_3$ sample was used for the determination of the instrumental contribution into

peak profile parameters. The data were further processed by Rietveld full-profile analysis using GSAS software [71]. The refinement yielded lattice periods of the constituent phases, their abundances, crystallite sizes and micro-strains. During refinements, Gaussian profile parameters (GU, GV and GW) were fixed (kept the same as for the Al_2O_3 standard), and only two Lorentzian profile parameters were refined, LX (size broadening) and LY (strain broadening).

The characteristics of the constituent phases were taken from CRYSTMET database [72], version 5.2.0, © Toth Information Systems, Inc. The following phases have been identified in the course of the XRD studies of all the samples:

- α-MgH_2: space group $P4_2/mnm$ (#136); a=4.4853 Å, c=2.9993 Å; ID: 506716.
- γ-MgH_2: space group $Pbcn$ (#60); a=4.4860 Å, b=5.4024 Å, c=4.8985 Å; ID: 506717.
- Mg: space group $P6_3/mmc$ (#194); a=3.2125 Å, c=5.2132 Å; ID: 455030.
- TiH_2: space group $Fm\,\overline{3}m$ (#225); a=4.465 Å; ID: 15440.

High-resolution transmission electron microscopy (HR-TEM), coupled with selected area electron diffraction (SAD) patterns, energy dispersive X-ray spectroscopy (EDS) and elemental mapping during electron energy loss spectroscopy (EELS) were used to investigate the structural, crystalline and compositional properties of the samples. The studies were carried out using a FEI Tecnai G^{2}20 field emission gun transmission electron microscope (FEG-TEM) operated at 200 kV.

For elemental mapping, the microscope was equipped with a Gatan Image Filter (GIF2001), which allows for electron energy loss spectroscopy (EELS) and energy filtered transmission electron microscopy (EFTEM). These techniques utilised the energy loss of electrons after interaction with the sample, as a finger-print tool to map the distribution of elements across the examined area. To determine the elemental composition of the specimens during the electron microscopy studies, site specific EDS was performed on various areas on the sample. The EDS spectra were collected using EDAX® liquid nitrogen cooled lithium-doped silicon (Si:Li) detector.

The powdered specimens were prepared for the electron microscopy experiments by dispersing approximately 1 mg of the sample powder in a 100 µL of pure ethanol, followed by ultrasonication for 5 minutes. One (approximately 5 µL) to two drops of solution were then drop-casted onto a holey carbon-coated Cu grid and finally placed for 10 minutes under a light source for the drying.

3. RESULTS AND DISCUSSION

3.1. Hydrogenation during HRBM.

Results showing hydrogen absorption in the studied samples during HRBM are presented in Figure 1 and Table 2. For the reference, the data for the individual Mg without additives (curve 1) and Mg + 5% C (curve 2) ball milled at the same conditions are presented in Figure 1 as well. The theoretical

amounts of the absorbed hydrogen (presented in brackets in the left column of Table 2) correspond to complete hydrogenation to yield MgH_2 and TiH_2, assuming that carbon in Mg + 5% C and $Mg_{0.9}Ti_{0.1}$ + 5% C is not hydrogenated during HRBM.

It is seen that HRBM of all the samples results in almost complete (94 to >98%) hydrogenation of Mg and Ti that corresponds to the final H/M values close to 2. The hydrogenation of Mg + 5% C and Mg requires 6 to 6.5 hours while at the presence of Ti the process completes in 40 minutes for $Mg_{0.5}Ti_{0.5}$ and in ~90 minutes for all other samples. The increase of Ti content in $Mg_{1-x}Ti_x$ results in a significant increase of the reaction rate constant, in ~3 times when x increases from 0 to 0.1 and, further in ~1.9 times when increasing x between 0.1..0.25 and 0.25..0.5. The Avraami exponent accordingly decreases from ~3 (x=0) to 1.8 (x=0.1) and further to 1.4 (x=0.25..0.5). It testifies about possible change of the reaction mechanism when the limiting process of phase transformation (n=2 or 3, depending on the mechanism of nucleation and dimensionality of the growth) is changed to diffusion (n=3/2, 5/2) [73].
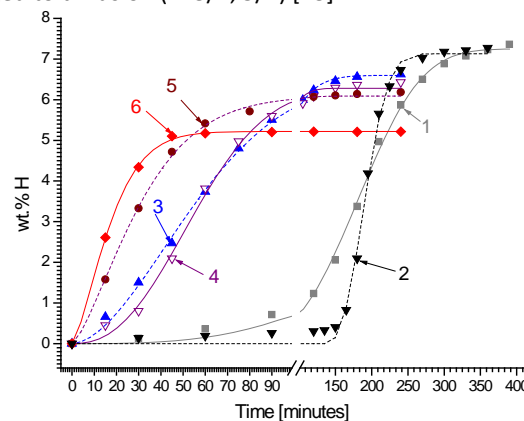

Figure 1. Hydrogen absorption during HRBM: experimental points and calculated curves. 1 – Mg, 2 – Mg + 5% C, 3 – $Mg_{0.9}Ti_{0.1}$, 4 – $Mg_{0.9}Ti_{0.1}$ + 5% C, 5 – $Mg_{0.75}Ti_{0.25}$, 6 – $Mg_{0.5}Ti_{0.5}$.

In presence of carbon the hydrogenation at the beginning of HRBM becomes slower (increase of n), but the fitted rate constant, k, remains almost the same. It significantly differs from the previously observed HRBM behaviour of individual Mg with 5 wt.% graphite when the hydrogenation was preceded by a quite long, >2 hours, incubation period ([52]; see also curve 2 in Figure 1). We believe that the improvement of the hydrogenation kinetics in $Mg_{0.9}Ti_{0.1}$ + 5% C as compared to Mg + 5% C has its origin in (i) increased ''scratching'' and milling of Mg (hardness 2.5 Mohs) and graphite (0.5–1 Mohs) particles assisted by Ti (6.0 Mohs) and/or TiH_2 (7.8 Mohs) and (ii) catalytic effect of Ti (or TiH_2 formed during HRBM) on the hydrogenation of Mg. Note that the kinetic improvements are mainly related to the disappearance of the incubation period while the fitted values of the rate constants and Avraami exponents do not significantly differ.

3.2. Dehydrogenation (TDS).

As it can be seen from *Supplementary Information, Figure S1*, hydrogen desorption from the as-milled materials takes place

in two stages. At the applied heating rate of 2 K min^{-1}, the first stage starts at T=130–160 °C and completes at T=270–307 °C corresponding to the decomposition of MgH$_2$. The second stage (decomposition of TiH$_2$) takes place in the temperature range from 402–420 °C to 533–575 °C. The temperatures of both onset and the end of the MgH$_2$ decomposition slightly

decrease with the increase of Ti content in the sample while TiH$_2$ decomposition exhibits reverse tendency. Introduction of graphite results in the widening of the corresponding peak which also widens as the content of Ti in the sample increases. For the sample Mg$_{0.5}$Ti$_{0.5}$ two overlapping peaks of the MgH$_2$ decomposition were clearly observed.

Table 2. Parameters of H absorption during HRBM.

Sample (wt.% H theoretical)	Milling time [min]	H absorption			Fitting parameters (Eq. 5)			
		wt.%H	Ncm^3/g	H/M	N_{max} [wt% H]	k [min^{-1}]	n	R^2
Mg (7.66)	390	7.36	890.2	1.91	7.25(9)	0.00486(6)	3.1(1)	0.9981
Mg + 5% C (7.29)	360	7.28	879.4	1.89	7.1(1)	0.016(4)[a]	2.6(7)	0.9963
Mg$_{0.9}$Ti$_{0.1}$ (7.03)	240	6.62	788.0	1.88	6.60(6)	0.0152(2)	1.79(6)	0.9987
Mg$_{0.9}$Ti$_{0.1}$ + 5%C (6.71)	240	6.43	763.4	1.91	6.28(8)	0.0158(3)	2.4(1)	0.9970
Mg$_{0.75}$Ti$_{0.25}$ (6.26)	240	6.18	732.3	1.97	6.09(4)	0.0287(6)	1.40(5)	0.9987
Mg$_{0.5}$Ti$_{0.5}$ (5.29)	240	5.21	611.2	1.97	5.22(2)	0.0513(7)	1.42(4)	0.9996

Note: [a] fitted value of incubation period t_0=135(15) min.

The total amount of the desorbed hydrogen is in a good correspondence with the data measured in the course of HRBM (Table 2) and varies from 96.6% (Mg$_{0.9}$Ti$_{0.1}$) to 99.2% (Mg$_{0.9}$Ti$_{0.1}$+5% C) of the theoretical hydrogen storage capacity. *Figure S2(A) in the Supplementary Information* shows an example of the TDS curves taken for Mg$_{0.9}$Ti$_{0.1}$+5% C at different heating rates; the Kissinger plots for all the samples are shown in *Figure S2(B)*.

As it can be seen from *Figure S2(B)* and Table 3, the TDS data are satisfactory fitted with Eq. 1; the values of Pearson correlation coefficient mostly correspond to R^2>0.99. HRBM Mg exhibits the slowest H$_2$ desorption kinetics with a typical value of the activation energy of about 150 kJ (mol H$_2$)$^{-1}$ that is in a good correspondence with the decomposition activation energy for ball milled MgH$_2$ retrieved from DSC data [46,68]. Addition of 5 wt.% of graphite (sample Mg + 5% C) results in some improvement of MgH$_2$ decomposition kinetics resulting in the lowering peak temperature by ~20 K and the decrease of the activation energy by 13% (see Table 3) that corresponds well to our earlier observations [52]. The value of the activation energy for Mg + 5% C (~130 kJ (mol H$_2$)$^{-1}$) is very close to the one measured for ball milled MgH$_2$ + 5% MWCNT (136 kJ (mol H$_2$)$^{-1}$ [46]).

Table 3. Parameters of H desorption during TDS.

Sample	T_m [°C] (β=2 K min^{-1})	E_A [kJ (mol H$_2$)$^{-1}$]	R^2
Mg	307	149(4)	0.9982
Mg + 5% C	286	129(3)	0.9980
Mg$_{0.9}$Ti$_{0.1}$	219	76(3)	0.9923
Mg$_{0.9}$Ti$_{0.1}$ + 5%C	236	88(2)	0.9982
Mg$_{0.75}$Ti$_{0.25}$	196	88(3)	0.9977
Mg$_{0.5}$Ti$_{0.5}$	189	91(7)	0.9819

At the same time, the samples containing Ti are characterised by a drastic improvement of the MgH$_2$ decomposition kinetics when the peak temperature at β=2 K min^{-1} decreases by about 100 K, and the activation energy is lowered in 1.6 to 2 times. Interesting, that the latter effect is more pronounced for the

samples with the lowest Ti concentration and is significantly higher than the effect of Co on the decrease of activation energy of MgH$_2$ decomposition in RBM MgH$_2$+Co(+MWCNT) [46]. Addition of 5 wt.% graphite to Mg$_{0.9}$Ti$_{0.1}$ results in insignificant increase of the peak temperature and the activation energy, but the improvements as compared to HRBM Mg and Mg + 5% C remain very high.

Figure 2 (A, C) shows TDS spectra taken for Mg$_{0.9}$Ti$_{0.1}$ (A) and Mg$_{0.9}$Ti$_{0.1}$+5% C (C) at different heating rates and "re-hydrogenation – TDS cycles". The experimental (points) and calculated (lines) spectra are in a satisfactory correspondence that testifies about applicability of the model [69] for the materials studied in this work. A comparison of the spectra taken at similar heating rates (~5 K min^{-1}) at the beginning (cycle 1) and the end (cycle 7) of the measurements show that in both cases H$_2$ desorption characteristics change with the cycling that results in the widening desorption peaks and decrease of their maxima.

Figure 2 (B, D) illustrates the changes of the rate dependence function with the cycle number. All $f(X)$ have a common feature and show presence of maxima that is a typical behaviour consistent with the reaction mechanism which involves nucleation and growth.

The heating rate does not significantly influence on the $f(X)$ behaviour (compare curves 4 and 5 in Figure 2B, D) but the changes are very pronounced on different re-hydrogenation – dehydrogenation cycles. It is seen that the increase of $f(X)$ with X in the ascending region becomes faster on the first 3–4 cycles whereupon the rate dependence functions become very close (cycles 4–7). Interesting, that the changes are much more pronounced for the carbon-containing sample (Figure 2D) when on the first 3 cycles the maximum of $f(X)$ is significantly shifted towards higher reacted fractions. Another feature of Mg$_{0.9}$Ti$_{0.1}$+5% C is a sharp growth of $f(X)$ at low X=0…0.015. Most probably, it is caused by a contribution of desorption of hydrogen bound by carbon additive during re-hydrogenation. This effect was found to be especially pronounced for Mg +

5%C as sharp leaps of $f(X)$ at X=0...0.01 followed by descending region at X<0.06 (see *Supplementary Information, Figure S3*). Dependencies of fitting parameters (Eq. 4) on the number of re-hydrogenation – dehydrogenation cycle are shown in *Supplementary Information, Figure S4*. A clear tendency of changing the reaction mechanism was observed as a significant change of the fitting parameters for both samples with the cycle number. For $Mg_{0.9}Ti_{0.1}$ (A), the parameters changed from M=1.16, N=1.88, P~0 on the first cycle to M~0, N=1.44, P=0.72 on the seventh one. The changes correspond to the change of rate-limiting process from growth of particles

during their precipitation determined by diffusion (P=0; M, N>0) to the nucleation and growth mechanism (equivalent to Avraami Eq. 5 at M=0, N=1, P<1)$^\$$. For $Mg_{0.9}Ti_{0.1}$ + 5% C (B), the observed change of the fitting parameters was from M=0.5, N=1.5, P=0.74 (cycle 1; the combination corresponds to a unidentified complicated mechanism [70]) to M=0.44, N=1, P~0 (cycle 7; growth of particles during their precipitation determined by diffusion). Here parameter M changed insignificantly (except for cycle 5 measured at the highest heating rate of 8 K min^{-1}) while N and P exhibited a clear trend to decrease.
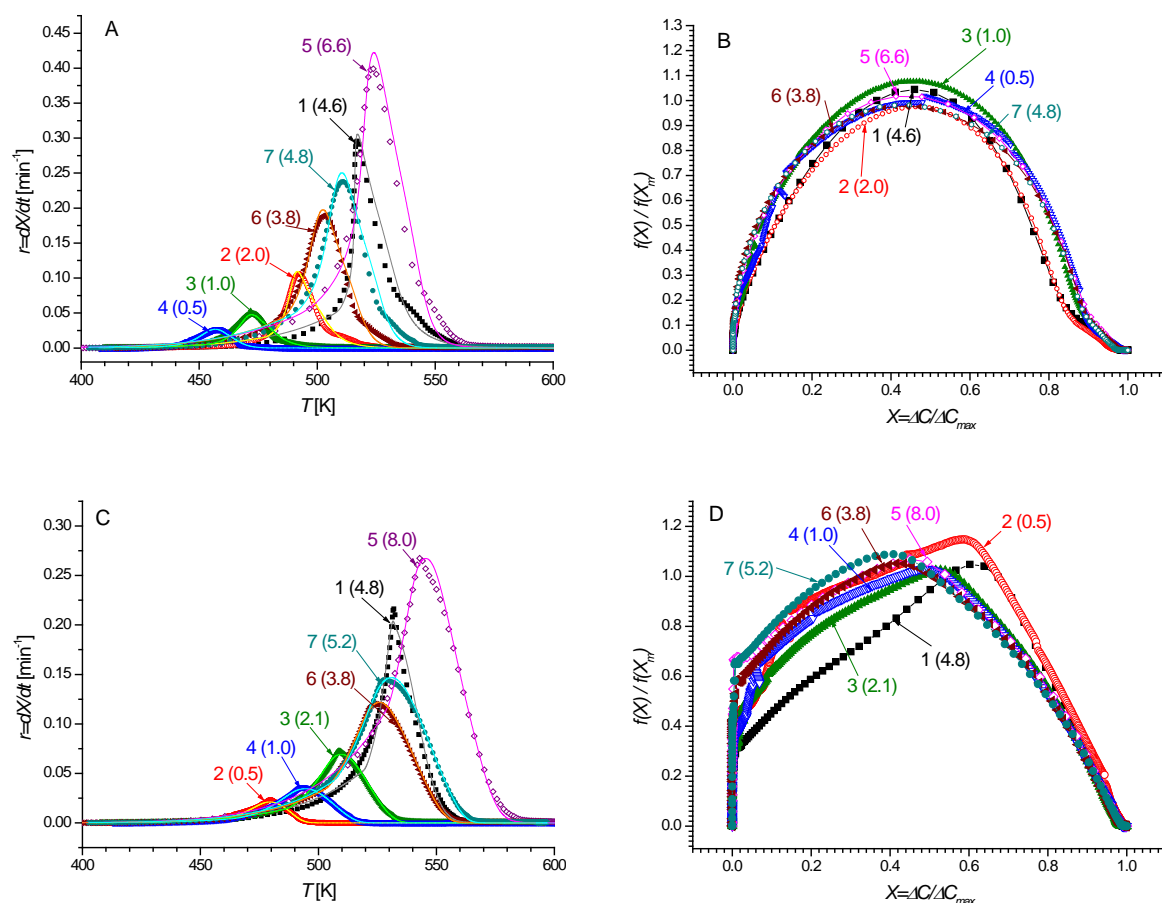
Figure 2. Experimental (points) and calculated (lines) thermal desorption spectra (A, C) and rate dependence functions (B, D) derived from the experimental TDS data. A, B – $Mg_{0.9}Ti_{0.1}$; C, D – $Mg_{0.9}Ti_{0.1}$ + 5% C. Curve captions correspond to cycle number followed by the average heating rate [K min^{-1}] (in brackets).

3.3. Re-hydrogenation and cycle stability.

Figure S5 in Supplementary Information shows kinetic curves for hydrogen absorption (A–C) and desorption (D–F) taken for the selected cycle numbers, in the course of the cycling stability studies (T=350 °C). Results of the fitting the experimental data are summarised in *in Supplementary information, Tables S2* (Eq. 6, absorption) and *S3* (Eq. 5, desorption). As it can be seen, at the experimental conditions the hydrogen desorption is faster than the absorption, and the absorption involves two processes: fast (k_1~1 min^{-1}) and slow (k_2~0.1 min^{-1}). Such a behaviour was observed in our earlier

publication [74] when processing hydrogenation kinetics for HRBM Mg derived from precise SR XRD data. The "fast" process was associated with nucleation and growth of MgH_2 while the "slow" one with H diffusion through growing hydride layer.

For the carbon-free MgH_2–TiH_2 materials both rate constants do not exhibit decrease with the cycling, and k_1 even increases by 20 ($Mg_{0.9}Ti_{0.1}$) to 40% ($Mg_{0.75}Ti_{0.25}$) during 30 and 40 cycles, respectively. At the same time, the contribution of the slow process (2) in the total hydrogen absorption kinetics significantly increases with the cycling of the carbon-free

An outstanding effect of graphite in nano-MgH$_2$-TiH$_2$ …   **Journal of Materials Chemistry A**

samples, and the total amount of the absorbed hydrogen, $N_{max}=A_1+A_2$, drops as well. As a result, during the cycling the reversible hydrogen storage capacity of the carbon-free materials significantly drops (Figure 3); this effect becomes more pronounced with the decrease of Ti content in the sample.

In contrast, the sample Mg$_{0.9}$Ti$_{0.1}$ + 5% C exhibits much higher cyclic stability. Despite of ~2 and ~1.5 times decrease of the rate constants for the hydrogenation (fast process) and dehydrogenation, respectively, the fraction, w_2, of the slow hydrogenation process even decreases in 5–10 times during the first 10 cycles and then remains approximately constant (Table 4). The reversible hydrogen storage capacity of Mg$_{0.9}$Ti$_{0.1}$ + 5% C drops by only 2% throughout 101 absorption/desorption cycle at T=350 °C while for the samples Mg$_{0.25}$Ti$_{0.25}$ and Mg$_{0.9}$Ti$_{0.1}$ the capacity drops by 13 and 43%, for 30 and 40 cycles, respectively (Figure 3).
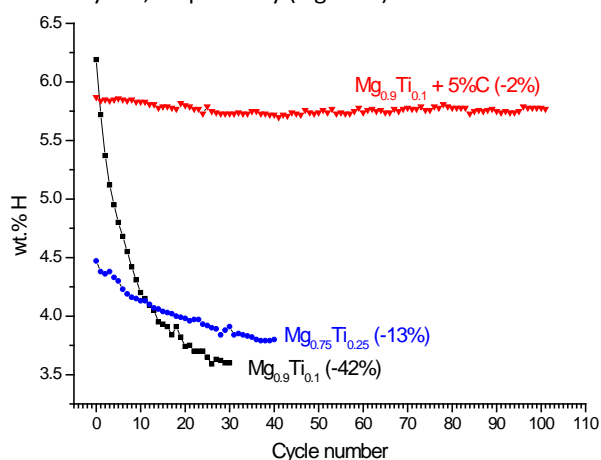
Figure 3. Reversible hydrogen storage capacity of the MgH$_2$–TiH$_2$ materials at T=350 °C. The values in brackets specify the capacity losses throughout the cycling.

Close values of the hydrogenation rate constants (k_1, fast process) for Mg$_{0.9}$Ti$_{0.1}$ and Mg$_{0.9}$Ti$_{0.1}$ + 5% C (Table S2), as well as faster dehydrogenation for Mg$_{0.9}$Ti$_{0.1}$ as compared to Mg$_{0.9}$Ti$_{0.1}$ + 5% C (Table S3) testify that the addition of graphite does not improve the hydrogenation and dehydrogenation

kinetics in MgH$_2$. This observation, together with the corresponding data on hydrogenation kinetics during HRBM (Section 3.1), as well as dehydrogenation kinetics during TDS (Section 3.2), confirms our hypothesis about absence of the direct catalytic effect of carbon on hydrogenation–dehydrogenation of Mg and suggestion that carbon plays a role of a carrier of the ''activated'' hydrogen by the spill-over [52]. At the same time, the carbon additive in Mg$_{0.9}$Ti$_{0.1}$ + 5% C results in the higher (in two times in average) rate constant, k_2, of the slow hydrogenation process and the decrease of its contribution in the overall hydrogenation kinetics during the cycling (Table S2). Thus the cycling stability of the carbon-containing sample is improved dramatically (Figure 3).

We note that all studied samples exhibited very good kinetics of hydrogen absorption taking place even at the room temperature and completing in less than 5 minutes at T=330 °C; see Figure 4A as example for Mg$_{0.9}$Ti$_{0.1}$ + 5% C. The activation energy for hydrogen absorption in this material was estimated as 47.3±0.4 kJ mol^{-1} (*see Supplementary Information, Figure S6*). This result is in a good correspondence with the value (41±2 kJ mol^{-1}) recently determined for the dehydrogenated material prepared by ball milling of MgH$_2$ with 5 mol% of nano-Fe; both values are significantly lower than the activation energy of Mg hydrogenation (70 kJ mol^{-1}) reported earlier [75].

At the same time, hydrogen absorption by the materials without carbon additives quickly deteriorates throughout the absorption/desorption cycling (see example in Figure 5). The changes are more pronounced for the low-temperature absorption when the amount of H$_2$ absorbed during 6 hours drops from 4.9 to 3.6 wt% when passing from the first to the fifth cycle (sample Mg$_{0.9}$Ti$_{0.1}$).

Conversely, the cycling of the sample Mg$_{0.9}$Ti$_{0.1}$ + 5% C does not result in the noticeable deterioration of the low-temperature H absorption kinetics during at least 50 re-hydrogenation – dehydrogenation cycles performed in this study (Figure 4B).
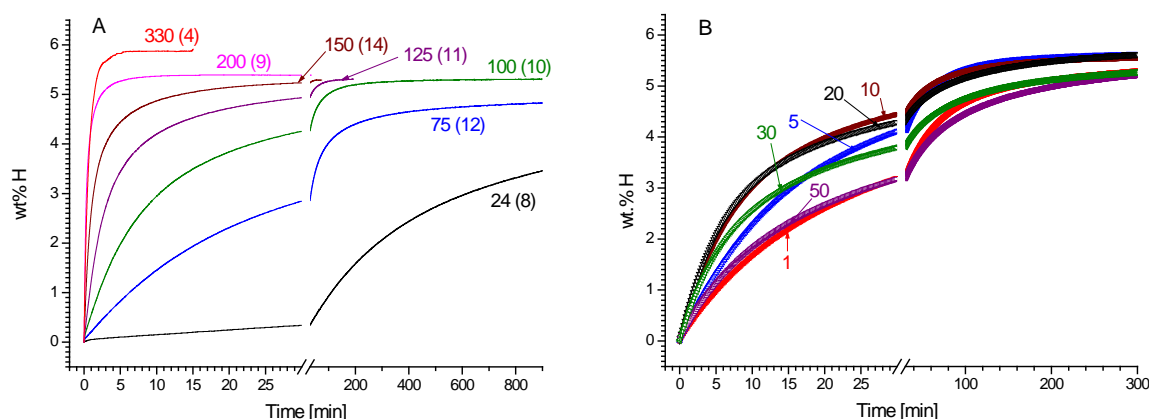

Figure 4. Hydrogen absorption kinetics for the sample Mg$_{0.9}$Ti$_{0.1}$ + 5% C. A – at different temperatures (the values in °C correspond to curve labels followed by the number of the absorption/desorption cycle in brackets); B – at T=100 °C; curve labels correspond to the number of the absorption/desorption cycle. The corresponding kinetic curves at T=200°C and 330 °C are presented in *Supplementary Information, Figure S7*.
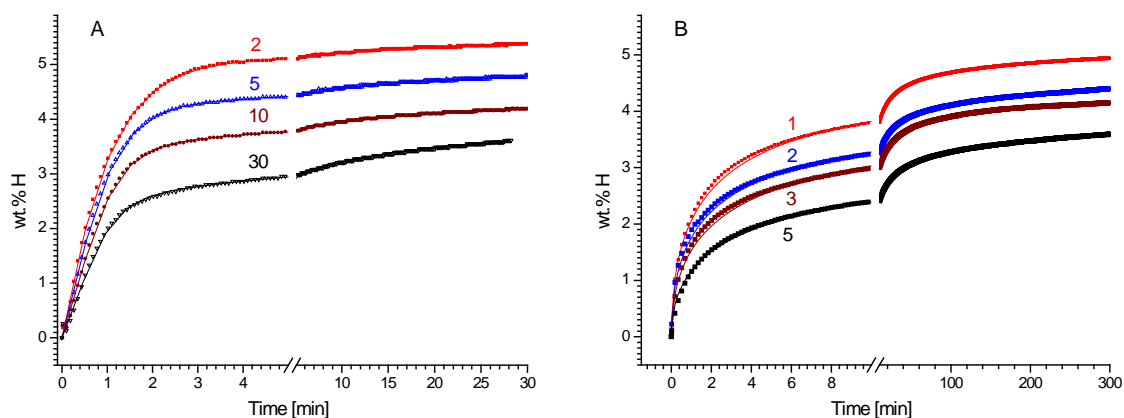
Figure 5. Hydrogen absorption kinetics for the sample $Mg_{0.9}Ti_{0.1}$ at T=350°C (A) and T=100°C (B). Curve labels correspond to the number of the absorption/desorption cycle.

Figure 6 shows the change of fitted kinetic parameters (Eq. 6) for $Mg_{0.9}Ti_{0.1}$ (A, B) and $Mg_{0.9}Ti_{0.1}$ + 5% C (C, D) with the cycle number at the temperature of 100°C; the calculated values of the fitting parameters are presented in *Supplementary Information, Table S4*, together with similar data for $Mg_{0.9}Ti_{0.1}$ + 5% C at the absorption temperatures of 200°C and 300 °C (*Figure S8*).

A comparison of the low-temperature H absorption data for $Mg_{0.9}Ti_{0.1}$ (Figure 6 A, B) and $Mg_{0.9}Ti_{0.1}$ + 5% C (Figure 6 C, D) shows dramatic differences between hydrogen absorption

kinetics in these two materials. For the carbon-free material (A, B), both "fast" (1) and "slow" (2) processes are characterised by the values of Avraami exponent, *n*, close to 0.5 unambiguously pointing to the diffusion-limiting mechanism. The value of the "slow" rate constant k_2 is very small, and the contribution of the "slow" process gradually increases (together with the decrease of k_1) with the cycle number. As a result, the maximum hydrogen absorption capacity drops by ~20% during the first five absorption / desorption cycles (see also Figure 5 B).
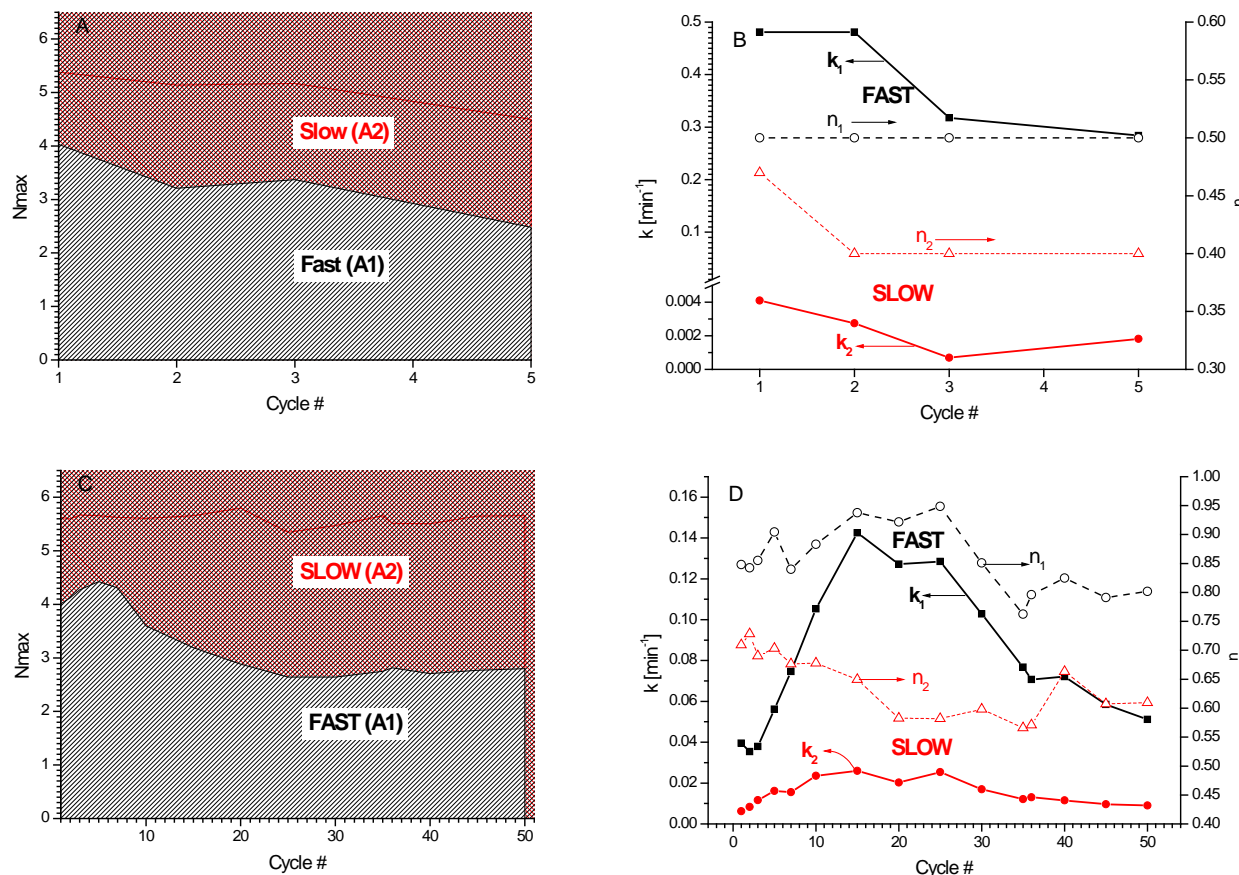
Figure 6. Change of kinetic parameters (Eq. 6) of H absorption during cycling for the samples $Mg_{0.9}Ti_{0.1}$ (A, B) and $Mg_{0.9}Ti_{0.1}$ + 5% C (C, D) at T=100°C.

Journal of Materials Chemistry A

ARTICLE

For $Mg_{0.9}Ti_{0.1}$ + 5% C (C, D), despite lower values of the rate constant k_1 and some reduction of the contribution of the "fast" hydrogenation process during the first twenty cycles, the overall kinetics even improves, first of all, due to significant increase of both rate constants, k_1 and k_2, corresponding to the "fast" and "slow" processes, respectively. Further cycling results in the slowing the kinetics down but the hydrogenation remains as fast as during the first cycle (see Figure 4B). The values of Avraami exponents change insignificantly (n_1=0.8–1.0, n_2=0.6–0.7) testifying that the hydrogenation mechanism remains approximately the same (nucleation and growth for both process, with a contribution of diffusion for the "slow" one). The hydrogenation kinetics at T=200 °C (*Figure S8 A, B*) is characterised by approximately equal contributions of the "fast" and "slow" processes ($A_1 \approx A_2$; also observed for T=100 °C after 20th cycle, Figure 6C). The kinetics slightly deteriorates after 15th cycle but remains very fast: about 5 wt% H is absorbing during 5 minutes. The ranges of variation of Avraami exponents (n_1=0.8–1.0, n_2=0.55–0.75) are similar to the ones for T=100 °C. At the same time, both n_1 and n_2 exhibited clear tendency of the decrease with the cycle number that testifies about gradual increase of the contribution of diffusion-related hydrogenation mechanism.

The high-temperature hydrogenation kinetics of the carbon-containing material (*Figure S8 C, D*) is characterised by a significant decrease of the contribution of the "slow" process (2) in the hydrogen absorption during the first ten cycles. This tendency is opposite to the one observed for the carbon-free samples (see *Supplementary Information*, *Table S4*) testifying about dramatic changes in the hydrogenation kinetics and mechanism upon introducing of a small amount of graphite in the composite.

3.4. XRD and TEM studies.

According to XRD results, the as-milled materials contain three nanocrystalline (10–20 nm) phases: TiH_2, α-MgH_2 and γ-MgH_2. After dehydrogenation at T<400 °C, the samples contain phases of Mg and TiH_2, and the re-hydrogenation results in the transformation of Mg into α-MgH_2. The lattice periods of the constituent phases are close to the corresponding reference data [72,74].

Table 4 shows summary of the XRD studies of the dehydrogenated samples $Mg_{0.9}Ti_{0.1}$ and $Mg_{0.9}Ti_{0.1}$ + 5% C (the XRD patterns are shown in *Supplementary Information, Figure S9*). The calculated weight abundances of TiH_2 in the not cycled samples are higher than the values calculated from stoichiometry of the samples: 20% for $Mg_{0.9}Ti_{0.1}$ (+9%) and 19% for $Mg_{0.9}Ti_{0.1}$ + 5% C (+37%). The cycled samples exhibit further increase of the calculated abundances of TiH_2: by 19% for $Mg_{0.9}Ti_{0.1}$ (30 cycles), but by only 4% for $Mg_{0.9}Ti_{0.1}$ + 5% C (105 cycles). The size of Mg crystallites for $Mg_{0.9}Ti_{0.1}$ increases in >4 times during the cycling. At the same time, $Mg_{0.9}Ti_{0.1}$ + 5% C which initially had 2.3 times bigger Mg crystallite size than the one in $Mg_{0.9}Ti_{0.1}$, exhibits the decrease of the size of Mg crystallites during the cycling. For all the samples, Mg crystallites do not exhibit strain. The phase of TiH_2 in all the samples exhibits crystallite size between 12 and 17 nm. The cycling of $Mg_{0.9}Ti_{0.1}$ results in the appearance of a significant strain in TiH_2 while for $Mg_{0.9}Ti_{0.1}$ + 5% C the initial strain significantly decreases during the cycling.

Table 4. Parameters of constituent phases in dehydrogenated samples $Mg_{0.9}Ti_{0.1}$ and $Mg_{0.9}Ti_{0.1}$ + 5% C.

Sample	Mg				TiH_2				Rp
	Abundance [wt.%]	a [Å]	c [Å]	Crystallite size [nm]	Abundance [wt.%]	a [Å]	Crystallite size [nm]	Strain [%]	
$Mg_{0.9}Ti_{0.1}$	78.2(-)	3.2002(8)	5.195(1)	28	21.8(6)	4.432(2)	12	0	0.0099
$Mg_{0.9}Ti_{0.1}$ (30 cycles)	74.1(-)	3.2057(4)	5.2056(8)	120	25.9(1)	4.431(2)	17	0.8	0.0090
$Mg_{0.9}Ti_{0.1}$ + 5% C	74(-)	3.2082(6)	5.207(1)	64	26(1)	4.437(2)	16	0.9	0.0093
$Mg_{0.9}Ti_{0.1}$ + 5% C (105 cycles)	73(-)	3.2079(7)	5.209(1)	28	27(5)	4.40(1)	13	0.2	0.0096

The characteristics regions on the HR TEM images for $Mg_{0.9}Ti_{0.1}$ where SAD patterns and EDS were taken are shown in *Supplementary Information, Figure S10*. The indexing of the SAD patterns corresponds to interplanar distances of the constituent phases (TiH_2 and Mg) identified by XRD (Table 4). As it can be seen, the sample contains irregularly shaped grains of various sizes varying between ~0.1 and 1 μ, with larger grains exhibiting a nanoscale twining (area 3). This morphology is typical for HRBM MgH_2 and its dehydrogenation products (see [68] and references therein). Ti content in the sample calculated from EDS (10.6 wt.%) shows underestimation as compared to the original sample composition (~18 wt.% Ti) that can be explained by segregation of Mg (probably, in the form of the surface oxide).

SAD patterns show that in the studied regions the sample consists of the mixture of micro-scale monocrystallites and

nano-scale polycrystallites; the latter were mainly observed in the twinning region (3). Elemental mapping (Figure 7, left) shows that Mg is uniformly distributed in the grains, and Ti (TiH_2) is clustered in the Mg matrix, with the cluster size up to 100 nm.
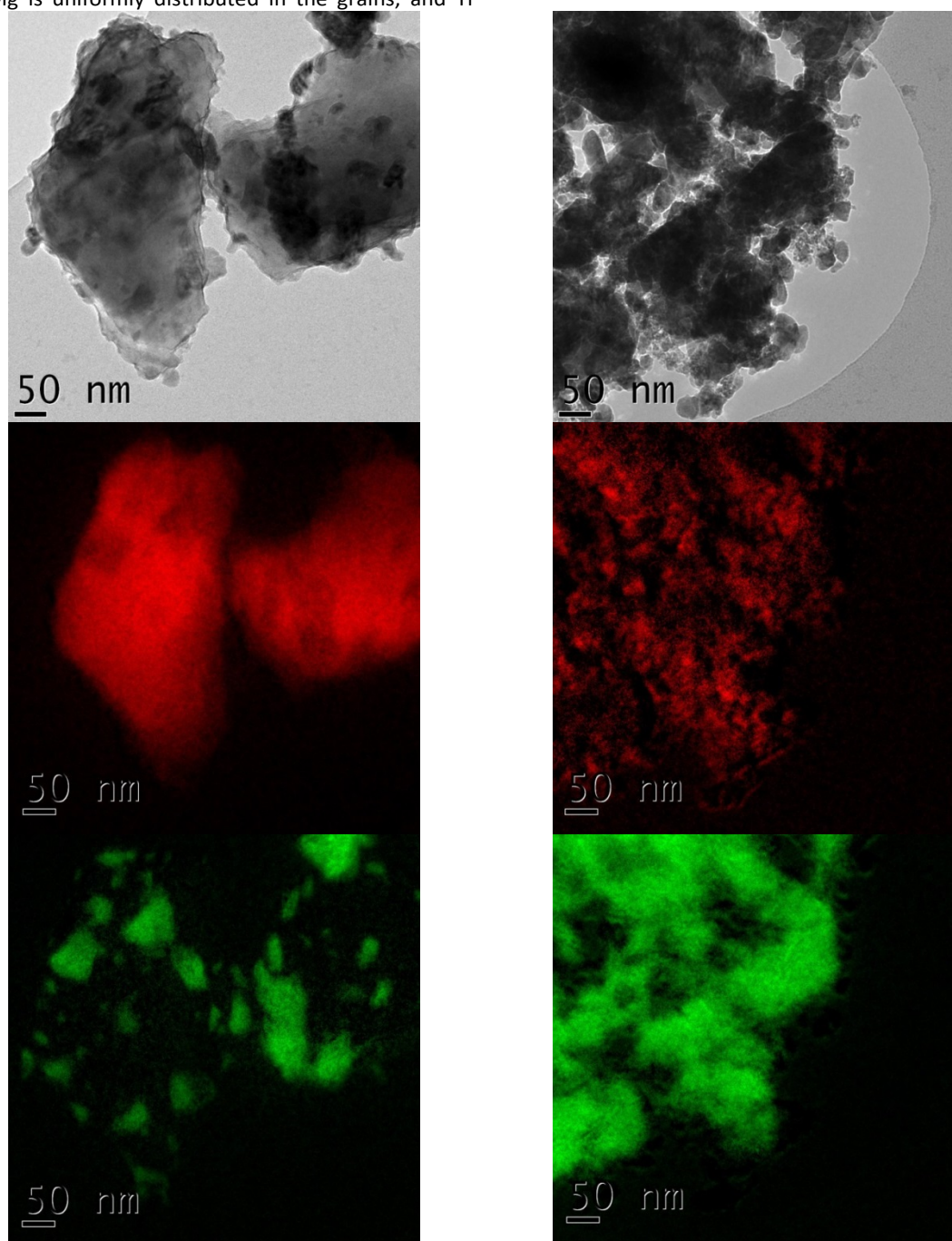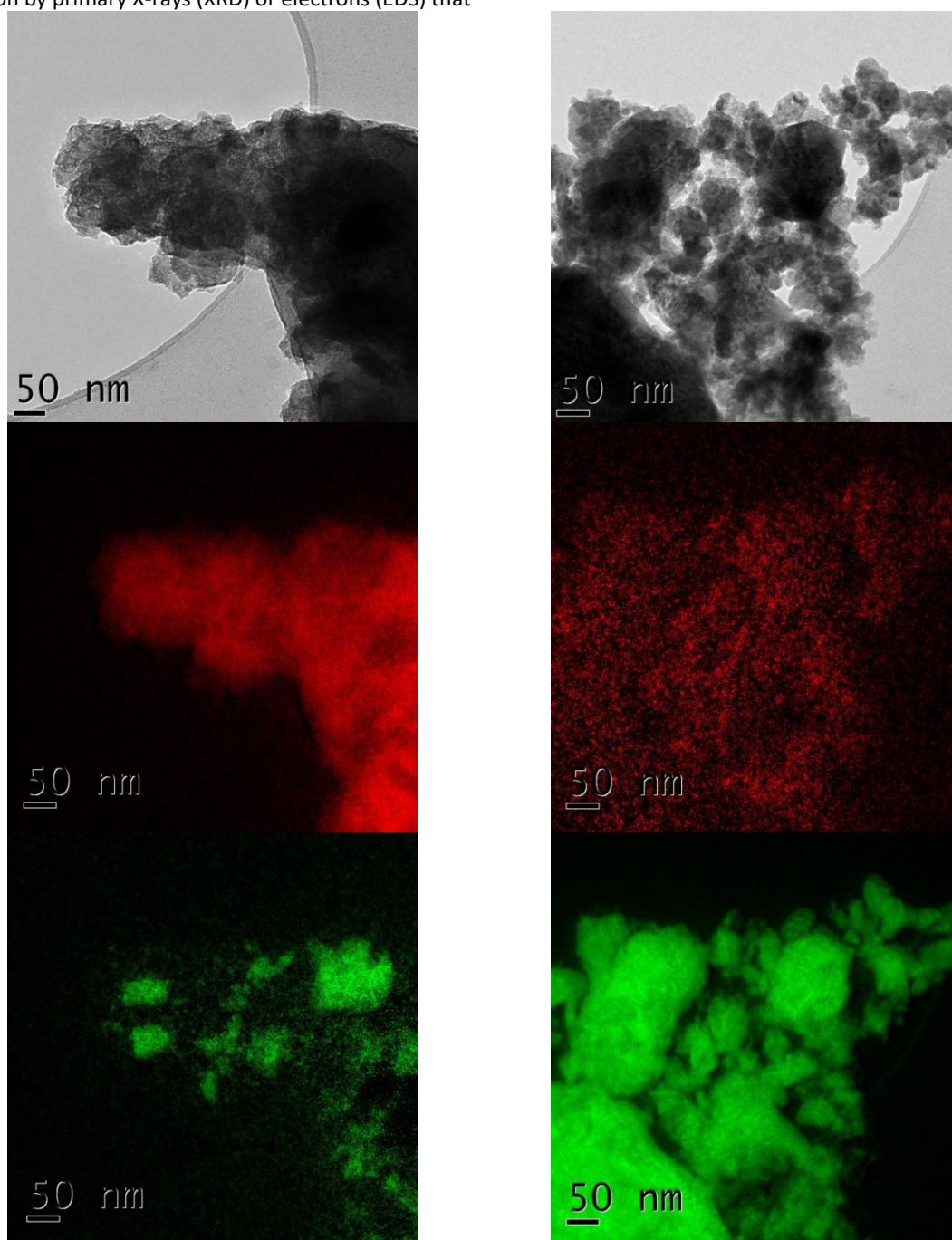

Figure 7. Elemental mapping of $Mg_{0.9}Ti_{0.1}$: left – before cycling, right – after 30 H absorption/desorption cycles. Top – filtered images, mid – Mg map (red), bottom – Ti map (green).

The HR TEM image of the cycled $Mg_{0.9}Ti_{0.1}$ (see *Supplementary Information, Figure S10*) exhibits higher amounts of the smaller (as compared to the non-cycled sample) particles (10 to 20 nm) which form agglomerates, most probably, sintered. The SAD patterns taken from areas 1–3 also exhibit the presence of the mixed polycrystallites and monocrystallites of both Mg and TiH_2. However, there are regions (3) where TiH_2 presents alone, preferably, in monocrystalline state.

XRD (Table 4) shows close values of the lattice periods for Mg and TiH_2 to the ones in the non-cycled sample, but with a significant increase in the Mg crystallite sizes and appearance of strain in TiH_2. Both XRD and EDS show significant increase in the calculated amount of TiH_2 to be 25.9 (XRD, Table 4), 31.4 (EDS 1) and 57.8 wt.% (EDS 2).

Elemental mapping (Figure 7, right) shows that Mg is uniformly distributed throughout the grains, together with dense clustering of Ti. From this observation we conclude that the

An outstanding effect of graphite in nano-MgH$_2$-TiH$_2$ …

cycling of Mg$_{0.9}$Ti$_{0.1}$ results in segregation and agglomeration of TiH$_2$ particles. Most probably, the segregation takes place around Mg particles which become surrounded by dense TiH$_2$ "pockets". By such a way, TiH$_2$ shields Mg particles weakening their irradiation by primary X-rays (XRD) or electrons (EDS) that

results in the increase of the ratio of secondary signals (TiH$_2$/Mg) and, in turn, the overestimation of TiH$_2$ concentration in the quantitative analysis.

Figure 8. Elemental mapping of Mg$_{0.9}$Ti$_{0.1}$+5%C: left – before cycling, right – after 105 H absorption/desorption cycles. Top – filtered images, mid – Mg map (red), bottom – Ti map (green).

According to the HR TEM images (see *Supplementary Information, Figure S12*), the sample Mg$_{0.9}$Ti$_{0.1}$+5% C before the cycling consists of micron-size agglomerates of particles (below 50 nm) which are smaller than for Mg$_{0.9}$Ti$_{0.1}$. Both SAD patterns (*Figure S12*) and XRD (Table 4) show presence of only Mg and TiH$_2$ with the lattice periods close to the reference data; no reflections from graphite were observed. Mostly, the

SAD patterns show presence of monocrystallites of Mg and TiH$_2$ (region 1 in *Figure S12*), while the other regions (## 2,3) show contribution of the nanoscale polycrystallites to the SADP.

Crystallite size (XRD, Table 4) of Mg phase in Mg$_{0.9}$Ti$_{0.1}$ + 5% C was calculated as 64 nm that is 2.3 times larger than for the sample Mg$_{0.9}$Ti$_{0.1}$ before cycling. TiH$_2$ crystallites have the size

(16 nm) that is close to the corresponding values for $Mg_{0.9}Ti_{0.1}$ without graphite additive before (12 nm) and after (17 nm) cycling. Significant strain, similar to the one for the cycled $Mg_{0.9}Ti_{0.1}$, was observed for TiH_2 in $Mg_{0.9}Ti_{0.1}$ + 5% C.

The abundances of TiH_2 according to the XRD (Table 4) and EDS taken from the regions 1 and 2 (*Figure S12*) were calculated as 26, 15.8 and 16.4 wt.%, respectively, indicating quite a good agreement with the EDS results and initial sample composition (~17 wt.% Ti). The carbon abundance calculated from the EDS data (10.2–12.5 wt.%) was overestimated in 2–2.5 times than can be explained by the contribution of holey-carbon grid holding the sample.

Elemental map (Figure 8, left) shows distributions of Mg and Ti similar to the ones in non-cycled $Mg_{0.9}Ti_{0.1}$ when TiH_2 forms clusters, up to 100 nm in the size, distributed over Mg matrix. Interesting that the graphite-containing sample shows a presence of a bigger amount of the smaller (below 10 nm) TiH_2 clusters whose distribution is quite uniform. The distribution of carbon (see *Supplementary Information, Figure S13*) was sparse and slightly interconnected. These observations confirm our previous conclusion [52] about encapsulation of hydride particles in carbon species (probably, stacked graphene layers) formed during RBM.

HR TEM images (see *Supplementary Information, Figure S14*) show that the cycled graphite-containing sample exhibits "friable" morphology represented by agglomerates, up to 100 nm in the size, of the smaller particles whose size can be estimated from Figure 8, top right, as <10 nm. XRD (Table 4) shows the presence of Mg and TiH_2 with lattice periods close to the reference data.

SADP (#2 in *Figure S14*) also shows presence of graphite with period c=6.963 Å that is 3.8% higher than the corresponding reference data ([72], ID: 131356; a=2.464 Å, c=6.711 Å). The patterns also show that the phases Mg and TiH_2 present in the sample as small-size monocrystallites (#1), or a mixture of the monocrystallites with nanoscale polycrystallites (#2).

XRD (Table 4) also shows very small crystallite sizes, 28 nm for Mg and 12 nm for TiH_2, that is lower than in the non-cycled $Mg_{0.9}Ti_{0.1}$ + 5%C. Cycling also results in the strain reduction in TiH_2, from 0.9 to 0.2%. According to both XRD (Table 4) and EDS ## 1 and 2 (*Figure S14*), $Ti(H_2)$ content in the sample is significantly overestimated calculated as 27, 60 and 53 wt.%, respectively. The EDS also show significant overestimation of the carbon content, 33 and 36 wt.% that exceeds the graphite content in the charge in more than 6 times.

Elemental mapping (Figure 8, right; *Figure S15 in Supplementary information*) shows scattered distribution of both Mg and C in the grains; Mg is observed on the map as very small, below 5-10 nm, spots uniformly distributed in the grains. It testifies that during the cycling Mg particles do not sinter but, quite opposite, are further refined. The carbon map (*Figure S15*, middle-right) exhibits a sparse distribution in the form of irregular mesh, preferably along grain boundaries and in between the grains. TiH_2, as in the case of the cycled $Mg_{0.9}Ti_{0.1}$ (Figure 7, right) forms clusters during the cycling. Interestingly, for the cycled $Mg_{0.9}Ti_{0.1}$+5%C (compare top-right and bottom-right images in Figure 8) the TiH_2 clusters

reproduce the shape of the grains. This, together with a significant overestimation of Ti content determined by EDS allows us to conclude that during the cycling of graphite-containing sample segregation of TiH_2 takes place at the grain surface.

Conclusions

This work employed experiments on Mg–Ti hydride composites containing from 50 to 90 at. % Mg as hydrogen storage materials operating at temperatures from 24 °C to 350 °C during hydrogen absorption and from 330 to 350 °C during hydrogen desorption. Particular focus was on a beneficial effect of graphite additive (5 wt. %) on the improvement of long term cycling stability of the composites allowing to achieve highly stable reversible H storage capacity of close to 6 wt. % H.

The studies of kinetics and mechanism of hydrogen absorption and desorption showed significant variation of the materials performance as related to the effect of graphite additive and cycling history of the materials.

This work showed that degradation of the reversible storage capacity of Mg-based Mg–Ti composites is strongly related to the operating temperature with a significant and rapid decline of the reversible capacity happening when it increases from normally used and reported in the reference data 300 °C, to a practically useful temperature level exceeding 330 °C utilised in current study. Particularly, severe degradation occurred when absorption of hydrogen was performed in the low temperature interval, ⩽200 °C.

However, addition of graphite, even at its modest content as low as 5 wt.%, allowed to mitigate such a behaviour achieving stable operation of the composite at 350 °C for at least 100 absorption – desorption cycles.

Kinetic modelling based on a modified Avraami equation for the H_2 absorption allowed to identify the mechanism of the processes explaining differences in the behaviour of the Mg–Ti and Mg–Ti–C composites. In particular, hydrogen absorption involves two processes, "fast" and "slow" ones, which contribute to the behaviours of every studied material, but their contribution is directly related to a number of parameters including:

    (a) presence or absence of graphite;

    (b) number of absorption-desorption cycles;

    (c) absorption temperature changing from 100 to 350 °C.

Modelling of the Thermal Desorption Spectra based on a modified Kissinger approach and combined form of differential kinetic equation showed that hydrogen desorption kinetics significantly changes with the number of the cycles even at the first cycling experiments, and these changes become much more significant for the graphite modified samples.

TEM studies (including SAD, EDS and elemental mapping) of the dehydrogenated samples of $Mg_{0.9}Ti_{0.1}$ and $Mg_{0.9}Ti_{0.1}$+5%C before and after the cycling at T=350 °C showed dramatic changes in distribution of Mg and TiH_2 after the cycling (segregation of TiH_2). Without graphite, the cycling results in the sintering/recrystallization of Mg which remains uniformly

distributed in the material. In presence of graphite, the cycling results in its further distribution in between the grains, as well as in between Mg nanoparticles which are further refined during the cycling. The Mg nanoparticles are uniformly distributed in the grains of the cycled material whose surface is covered by the segregated TiH$_2$.

As a result, the addition of carbon (graphite) in the amount as low as 5 wt.% to MgH$_2$–TiH$_2$ nanostructured materials allows to avoid deterioration of their hydrogen sorption performance during cyclic hydrogen absorption/desorption at high temperatures.

Conflicts of interest

There are no conflicts to declare.

Acknowledgements

Notes

* In all experiments related to H$_2$ absorption / desorption cycling, the cycles were counted starting from the first re-hydrogenation. TDS data for the as-milled samples (cycle 0) were not processed due to the fact that the as-milled samples contained a mixture of α- and γ-modifications of MgH$_2$ resulting in the changes of the TDS behaviour while the next dehydrogenations involved a contribution from α-MgH$_2$ only.

§ Assuming $\Delta S^0 = -141.2$ J mol^{-1} K^{-1} and $\Delta H^0 = -78.9$ kJ mol^{-1}, the calculated plateau pressure for MgH$_2$ at T=350 °C will be equal to 5.78 bar that is in between the starting and final hydrogen pressures after H$_2$ absorption and desorption, respectively.

For the sample Mg + 5% C the HRBM kinetic data was processed by a modified Avraami – Erofeev equation (Eq. 1 in [52]), with incubation period, t_0, and characteristic hydrogenation time, $t_R=1/k$.

\$ The value of the exponential factor can be calculated as $n = \frac{1}{1-P}$ [69]. At $P<0$ ($n<1$), the mechanism is associated with diffusion [73].

References

1 P. Selvam, B. Viswanathan, C. S. Swamy and V. Srinivasan, *Int. J. Hydrogen Energy*, 1986, **11**, 169.

2 B. Sakintuna, F. Lamari-Darkrim and M. Hirscher, *Int. J. Hydrogen Energy*, 2007, **32**, 1121.

3 I.P. Jain, C. Lal and A. Jain, *Int. J. Hydrogen Energy*, 2010, **35**, 5133.

4 J.-C. Crivello, B. Dam, R.V. Denys, M. Dornheim, D.M. Grant, J. Huot, T.R. Jensen, P. de Jongh, M. Latroche, C. Milanese, D. Milčius, G.S. Walker, C.J. Webb, C. Zlotea and V.A. Yartys, *Appl. Phys. A*, 2016, **122**, 97.

5 B. Bogdanović, A. Ritter, B. Spliethoff and K. Strassburger, *Int. J. Hydrogen Energy*, 1995, **20**, 811.

6 A. Reiser, B. Bogdanović and K. Schlichte, *Int. J. Hydrogen Energy* 2000, **25**, 425.

7 J.-C. Crivello, R. V. Denys, M. Dornheim, M. Felderhoff, D.M. Grant, J. Huot, T.R. Jensen, P. de Jongh, M. Latroche, G.S. Walker, C.J. Webb and V.A. Yartys, *Appl. Phys. A* 2016, **122**, 85.

8 V.A. Yartys, V.E. Antonov, S.V. Mitrokhin and V.N. Verbetsky, *J. Alloys Compds*, 2011, **509S**, S515.

9 Y. Kojima, Y. Nakamura and S-I. Orimo, *J. Alloys Compds*, 2013, **580**, S1.

10 G.S. Walker, *J. Alloys Compds*, **645** (2015) S1.

11 *15th International Symposium on Metal-Hydrogen Systems (MH2016)*, https://mh2016.ch/

12 A. Zaluska, L. Zaluski and J.O. Ström–Olsen, *J. Alloys Compds*, 1999, **288**, 217.

13 G. Liang, J. Huot, S. Boily, A. Van Neste and R. Schulz, *J. Alloys Compds*, 1999, **292**, 247.

14 Z. Dehouche, R. Djaozandry, J. Huot, S. Boily, J. Goyette, T.K. Bose and R. Schulz, *J. Alloys Compds*, 2000, **305**, 264.

15 W. Oelerich, T. Klassen and R. Bormann, *J. Alloys Compds*, 2001, **322**, L5.

16 J. Charbonnier, P. de Rango, D. Fruchart, S. Miraglia, L. Pontonnier, S. Rivoirard, N. Skryabina and P. Vulliet, *J. Alloys Compds*, 2004, **383**, 205.

17 N. Hanada, T. Ichikawa and H. Fujii, *J. Phys. Chem. B*, 2005, **109**, 7188.

18 H.G. Schimmel, J. Huot, L.C. Chapon, F.D. Tichelaar and F.M. Mulder, *J. Am. Chem. Soc.*, 2005, **127**, 14348.

19 M.V. Lototsky, R.V. Denys and V.A. Yartys, *Int. J. Energy Research*, 2009, **33**, 1114.

20 Y. He, J. Fan and Y. Zhao, *Int. J. Hydrogen Energy*, 2010, **35**, 4162

21 B.S. Amirkhiz, B. Zahiri, P. Kalisvaart and D. Mitlin, *Int. J. Hydrogen Energy*, 2011, **36**, 6711.

22 H.Gasan, O.N. Celik, N. Aydinbeyli and Y.M. Yaman, *Int. J. Hydrogen Energy*, 2012, **37**, 1912.

23 A.S. Awad, E. El-Asmar, T. Tayeh, F. Mauvy, M. Nakhl, M. Zakhour and J.-L. Bobet, *Energy*, 2016, **95**, 175.

24 M.P. Pitt, M. Paskevicius, C.J. Webb, D.A. Sheppard, C.E. Buckley and E. MacA. Gray, *Int. J. Hydrogen Energy*, 2012, **37**, 4227.

25 C. Zhou, Z.Z. Fang and R.C. Bowman, Jr., *J. Phys. Chem. C,* 2015, **119**, 22261.

26 C. Zhou, Z.Z. Fang, R.C. Bowman, Jr., Y. Xia, J. Lu, X. Luo and Y. Ren, *J. Phys. Chem. C*, 2015, **119**, 22272.

27 G. Barkhordarian, T. Klassen and R. Bormann, *J. Alloys Compds*, **2004**, 364, 242.

28 K.S. Jung, E.Y. Lee and K.S. Lee, *J. Alloys Compds*, 2006, **421**, 179.

29 M. Polanski, J. Bystrzycki, R.A. Varin, T. Plocinski and M. Pisarek, *J. Alloys Compds*, 2011, **509**, 2386.

30 M.S. El-Eskandarany, E. Shaban and A. Al-Shemmiri, *Int. J. Hydrogen Energy*, **2014**, 39, 21097

31 M. Lototskyy, M.W. Davids, J.M. Sibanyoni, J. Goh and B.G. Pollet, *J. Alloys Compds*, 2015, **645**, S454.

32 A. Bhatnagar, S.K. Pandey, A. Vishwakarma, S. Singh, V. Shukla, P.K. Soni, M.A. Shaz and O.N. Srivastava, *J. Mater. Chem. A*, 2016, **4**, 14761.

33 H. Shao, M. Felderhoff and F. Schüth, *Int. J. Hydrogen Energy*, 2011, **36**, 10828.

34 J. Lu, Y.J. Choi, Z.Z. Fang, H.Y. Sohn and E. Rönnebro, *J. Am. Chem. Soc.*, 2009, **131**, 15843.

35 H.Y. Sohn and S. Emami, *Int. J. Hydrogen Energy*, 2011, **36**, 8344

ARTICLE

36 Y.J. Choi, J. Lu, H.Y. Sohn and Z.Z. Fang, *J. Power Sources*, 2008, **180**, 491.

37 Y.J. Choi, J. Lu, H.Y. Sohn, Z.Z. Fang and E. Rönnebro, *J. Phys. Chem. C*, 2009, **113**, 19344.

38 N. Patelli, M. Calizzi, A. Migliori, V. Morandi and L. Pasquini, *J. Phys. Chem. C*, 2017, **121**, 11166.

39 X. Ding, Y. Li, F. Fang, D. Sun and Q. Zhang, *J. Mater. Chem. A*, 2017, **5**, 5067.

40 H. Imamura, M. Kusuhara, S. Minami, M. Matsumoto, K. Masanari, Y. Sakata, K. Itoh and T. Fukunaga, *Acta Mater.*, 2003, **51**, 6407.

41 J.-L. Bobet, E. Grigorova, M. Khrussanova, M. Khristov, P. Stefanov, P. Peshev and D. Radev, *J. Alloys Compds*, 2004, **366**, 298.

42 D.L. Narayanan and A.D. Lueking, *Carbon*, 2007, **45**, 805.

43 M.A. Lillo-Ródenas, Z.X. Guo, K.F. Aguey-Zinsou, D. Cazorla-Amorós and A. Linares-Solano, *Carbon*, 2008, **46**, 126.

44 T. Spassov, Z. Zlatanova, M. Spassova and S. Todorova, *Int. J. Hydrogen Energy*, 2010, **35**, 10396.

45 A. Ranjbar, M. Ismail, Z.P. Guo, X.B. Yu and H.K. Liu, *Int. J. Hydrogen Energy*, 2010, **35**, 7821.

46 M.G. Verón, H. Troiani and F.C. Gennari, *Carbon*, 2011, **49**, 2413.

47 V. Fuster, F.J. Castro, H. Troiani and G. Urretavizcaya, *Int. J. Hydrogen Energy*, 2011, **36**, 9051.

48 A.D. Rud and A.M. Lakhnik, *Int. J. Hydrogen Energy*, 2012, **37**, 4179.

49 Y. Jia, Y. Guo, J. Zou and X. Yao, *Int. J. Hydrogen Energy*, 2012, **37**, 7579.

50 Y. Jia, J. Zou and X. Yao, *Int. J. Hydrogen Energy*, 2012, **37**, 13393.

51 A. Kubota, H. Miyaoka, M. Tsubota, K. Shimoda, T. Ichikawa and Y. Kojima, *Carbon*, 2013, **56**, 50.

52 M. Lototskyy, J.M. Sibanyoni, R.V. Denys, M.Williams, B.G. Pollet and V.A. Yartys, *Carbon*, 2013, **57**, 146.

53 S. Zhou, H. Chen, W. Ran, N. Wang, Z. Han, Q. Zhang, X. Zhang, H. Niu, H. Yu and D. Liu, *J. Alloys Compds*, 2014, **592**, 231.

54 S. Zhou, X. Zhang, T. Li, N. Wang, H. Chen, T. Zhang, H. Yu, H. Niu and D. Liu, *Int. J. Hydrogen Energy*, 2014, **39**, 13628.

55 Y.Huang, G.Xia, J.Chen, B.Zhang, Q.Li and X.Yu, *Progr. Natur. Sci.: Mater. Int.*, 2017, **27**, 81.

56 J. Cui, J. Liu, H. Wang, L. Ouyang, D. Sun, M. Zhu and X. Yao, *J. Mater. Chem. A*, 2014, **2**, 9645.

57 A. Jain, S. Agarwal, S. Kumar, S. Yamaguchi, H. Miyaoka, Y. Kojima and T. Ichikawa, *J. Mater. Chem. A*, 2017, **5**, 15543.

58 C. Zhou, Z.Z. Fang and P. Sun, *J. Power Sources*, 2015, **278**, 38.

59 J. Zhang, S. Yan and H. Qu, *Int. J. Hydrogen Energy*, 2018, **43**, 1545.

60 G. Stepura, V. Rosenband and A. Gany, *J. Alloys Compds*, 2012, **513**, 159.

61 M.V. Lototskyy, I. Tolj, L. Pickering, C. Sita, F. Barbir and V.Yartys, *Progr. Natur. Sci.: Mater. Int.*, 2017, **27**, 3.

62 M. Lototskyy, S. Nyallang Nyamsi, S. Pasupathi, I. Wærnhus, A. Vik, C. Ilea and V. Yartys, in: *2nd Int. Symp. on Materials for Energy Storage and Conversion, Ortahisar, Cappadocia, Turkey, Sept. 25-28, 2017; mESC-IS2017, Abstracts*, p.92.

63 W.P. Kalisvaart, C.T. Harrower, J. Haagsma, B. Zahiri, E.J. Luber, C. Ophus, E. Poirier, H. Fritzsche and D. Mitlin, *Int. J. Hydrogen Energy*, 2010, **35**, 2091.

64 E. Ruse, M. Buzaglo, I. Pri-Bar, L. Shunak, R. Nadiv, S. Pevzner, O. Siton-Mendelson, V.M. Skripnyuk, E. Rabkin and O. Regev, *Carbon*, 2018, **130**, 369.

65 Y. Wang, C. An, Y. Wang, Y. Huang, C. Chen, L. Jiao and H. Yuan, *J. Mater. Chem. A*, 2014, **2**, 16285.

66 H.E. Kissinger, *Anal. Chem.*, 1957, **29**, 1702.

67 R.L. Blaine and H.E. Kissinger, *Thermochim. Acta*, 2012, **540**, 1.

68 M. Danaie, S.X.Tao, P. Kalisvaart and D.Mitlin, *Acta Mater.*, 2010, **58**, 3162.

69 M. Lototskyy, R. Denys, S. Nyallang Nyamsi, I. Bessarabskaia and V. Yartys, *Mater. Today: Proc.*, in press, DOI 10.1016/j.matpr.2017.12.375.

70 J. Šesták, G. Berggren, *Thermochim. Acta*, 1971, **3**, 1.

71 A.C. Larson and R.B. Von Dreele, *Los Alamos Nat. Lab. Rep.*, 2004, **LAUR 86-748**.

72 P.S. White, J.R. Rodgers and Y. Le Page, *Acta Cryst.*, 2002, **B 58**, 343.

73 T. Førde, J.P. Maehlen, V.A.Yartys, M.V. Lototsky and H. Uchida, *Int. J. Hydrogen Energy*, 2007, **32**, 1041.

74 R.V. Denys, A.B. Riabov, J.P. Maehlen, M.V. Lototsky, J.K. Solberg and V.A. Yartys, *Acta Mater.*, 2009, **57**, 3989.

75 S. Kumar, A. Singh, G.P. Tiwari, Y. Kojima and V. Kain, *Thermochim. Acta*, 2017, **652**, 103.

Supplementary information to the paper

AN OUTSTANDING EFFECT OF GRAPHITE IN NANO-MgH$_2$-TiH$_2$ ON HYDROGEN STORAGE PERFORMANCE

by M. Lotoskyy, R. Denys, V.Yartys, J. Eriksen, J. Goh, S. Nyallang Nyamsi, C. Sita, and F. Cummings

Table S1. Summary of experimental conditions of kinetic studies ("low-temperature" H absorption)

A. Mg$_{0.9}$Ti$_{0.1}$:

Cycle No.	Absorption				Desorption			
	T, °C	P_0, bar	P_f, bar	ΔCmax, wt.%	T, °C	P_0, bar	P_f, bar	ΔCmax, wt.%
0					330	0.001	0.23	6.3
1	100	10.25	5.5	5.19	330	0.19	0.40	5.58
2	100	10.2	5.9	4.74	330	0.2	0.39	5.29
3	100	10.3	6.2	4.5	330	0.2	0.39	5.04
4	330	10	8.9	5.82	330	1.05	2.14	5.95
5	100	10.3	6.65	4.01	330	0.22	0.38	4.78

B. Mg$_{0.9}$Ti$_{0.1}$ + 5% C:

Cycle No.	Absorption				Desorption			
	T, °C	P_0, bar	P_f, bar	ΔCmax, wt.%	T, °C	P_0, bar	P_f, bar	ΔCmax, wt.%
0					330	0.001	0.235	5.96
1	100	10.3	4.7	5.58	330	0.19	0.42	5.78
2	100	10.4	4.8	5.6	330	0.19	0.42	5.77
3	100	10.5	4.7	5.68	330	0.19	0.42	5.78
4	330	10	8.7	6.01	330	1.0	2.2	5.97
5	100	10.5	4.8	5.67	330	0.19	0.42	5.78
6	150	10.5	4.7	5.74	330	0.19	0.42	5.79
7	100	10.4	4.8	5.64	330	0.19	0.42	5.78
8	24	10.3	5.5	4.85	330	0.18	0.41	5.79
9	200	10.4	4.5	5.89	330	0.19	0.42	5.80
10	100	10.5	4.8	5.62	330	0.2	0.42	5.77
11	125	10.4	4.7	5.75	330	0.19	0.42	5.77
12	75	10.3	5.1	5.23	330	0.19	0.42	5.75
13	125	10.4	4.7	5.65	330	0.19	0.42	5.80
14	150	10.4	4.8	5.60	330	0.2	0.42	5.78
15	100	10.35	6.67	5.65	330	1	2.20	5.94[1]
16	200	10.25	4.45	5.93	330	0.18	0.40	5.79
17	50	10.24	5.32	4.96	330	0.2	0.41	5.77
18	135	10.5	4.69	5.76	330	0.2	0.44	5.84
19	170	10.5	4.68	5.80	330	0.19	0.41	5.77
20	100	10.33	4.495	5.79	330	0.19	0.41	5.73
21	120	10.53	4.797	5.69	330	0.2	0.427	5.74
22	80	10.37	5.152	5.23	330	0.19	0.417	5.73
23	140	10.36	4.563	5.75	330	0.188	0.413	5.74
24	160	10.5	4.647	5.84	330	0.189	0.415	5.74
25	100	10.34	4.948	5.35	330	0.2	0.415	5.71

(to be continued)

[1] After holding the sample at the H$_2$ pressure and room temperature for 1 week

Table S1 (B) – continued

Cycle No.	Absorption				Desorption			
	T, °C	P_0, bar	P_f, bar	ΔCmax, wt.%	T, °C	P_0, bar	P_f, bar	ΔCmax, wt.%
26	180	10.48	4.684	5.81	330	0.181	0.407	5.77
27	330	9.9	8.6	6.01	330	1.04	2.21	5.94
28	220	10.5	4.62	5.93	330	0.192	0.416	5.76
29	200	10.5	4.48	5.92	330	0.189	0.414	5.75
30	100	10.42	4.9	5.47	330	0.065	0.29	5.75
31	350	10.3	9.1	6.01	350	0.12	0.35	5.83
32	320	10.3	9.1	6.01	320	0.12	0.35	5.84
33	300	10.2	9.0	6.0	300	0.12	0.35	5.83
34	280	10.2	9.0	5.97	280	0.12	0.35	5.83
35	100	10.41	4.725	5.64	330	0.181	0.401	5.69
36	100	10.38	4.88	5.51	330	0.188	0.41	5.66
37	330	9.9	8.7	5.97	330	1.04	2.22	5.97
38	330	10.1	8.85	6.01	330	1.04	2.22	5.98
39	200	10.6	4.6	5.92	330	0.188	0.413	5.75
40	100	10.39	4.865	5.49	330	0.185	0.406	5.65
41	330	10	8.8	6.02	330	1.06	2.24	5.97
42	330	10	8.8	5.98	330	1.04	2.21	5.96
43	330	10.1	8.9	5.97	330	1.04	2.22	5.96
44	330	10	8.8	5.99	330	1.04	2.22	5.95
45	100	10.5	4.84	5.62	330	0.189	0.412	5.65
46	330	9.9	8.68	6.02	330	1.04	2.22	5.94
47	330	10	8.8	5.99	330	1.04	2.22	5.95
48	330	10	8.8	5.97	330	1.04	2.22	5.97
49	200	10.5	4.56	5.93	330	0.191	0.416	5.73
50	100	10.33	4.65	5.63	Unloaded in the hydrogenated state			
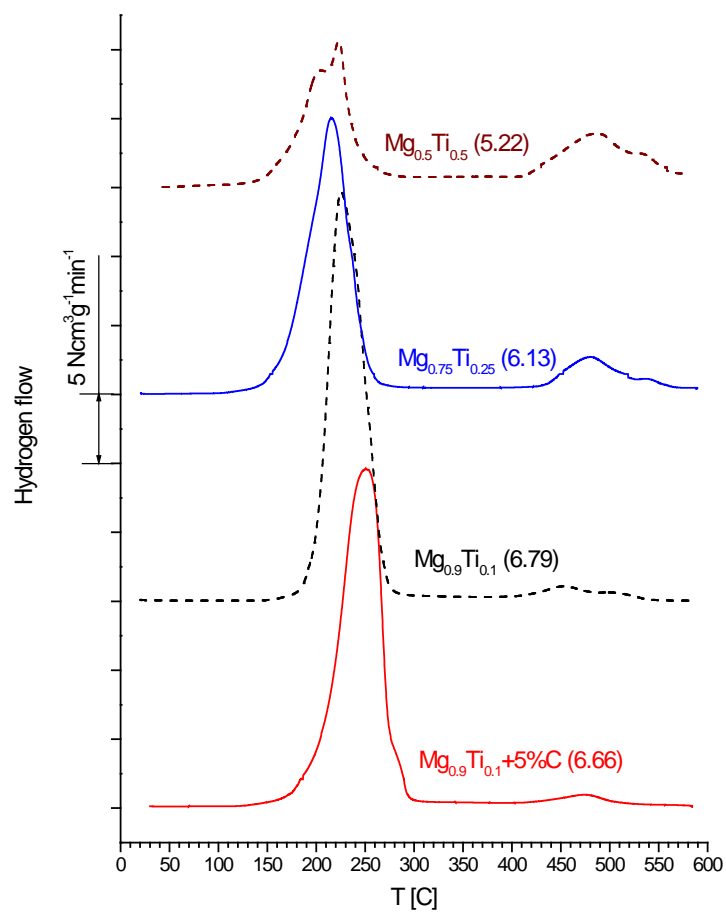
Figure S1. TDS curves for the as-prepared materials. The values in brackets next to curve labels specify the total amounts of hydrogen [wt.%] desorbed from the samples.
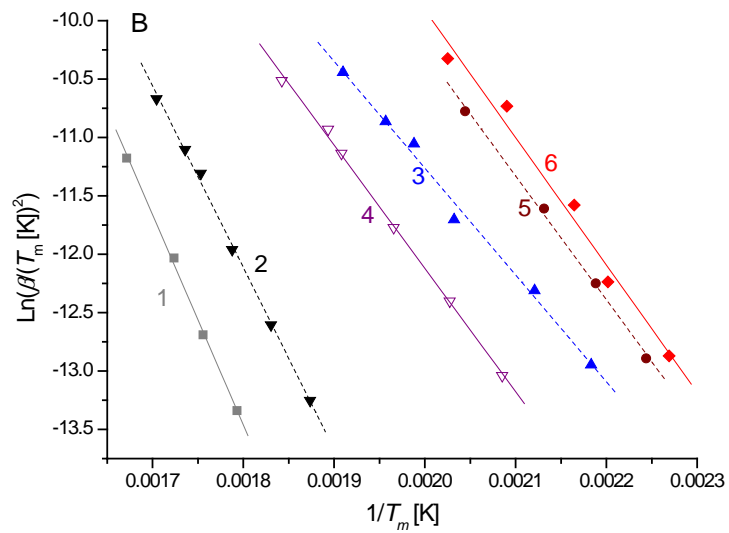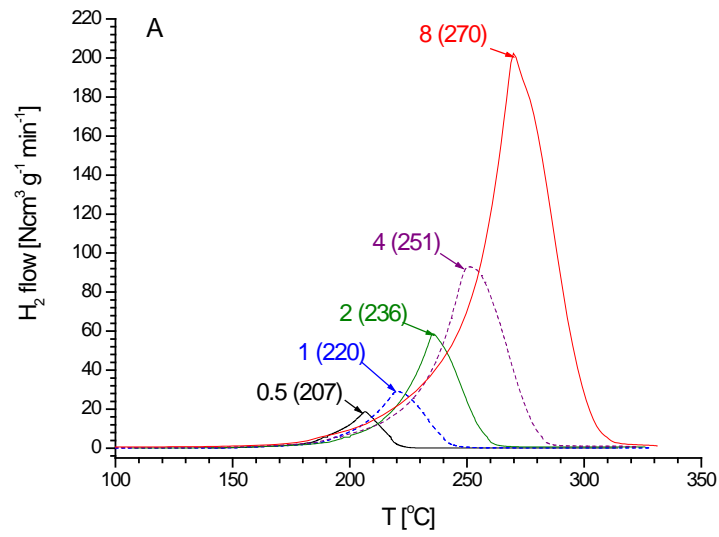
Figure S2. A – TDS curves for Mg$_{0.9}$Ti$_{0.1}$+5% C; curve labels correspond to the heating rates [K min^{-1}] followed by the peak temperature [^{o}C] in brackets. B – Kissinger plots for Mg (1), Mg + 5% C (2), Mg$_{0.9}$Ti$_{0.1}$ (3), Mg$_{0.9}$Ti$_{0.1}$ + 5% C (4), Mg$_{0.75}$Ti$_{0.25}$ (5), and Mg$_{0.5}$Ti$_{0.5}$ (6).
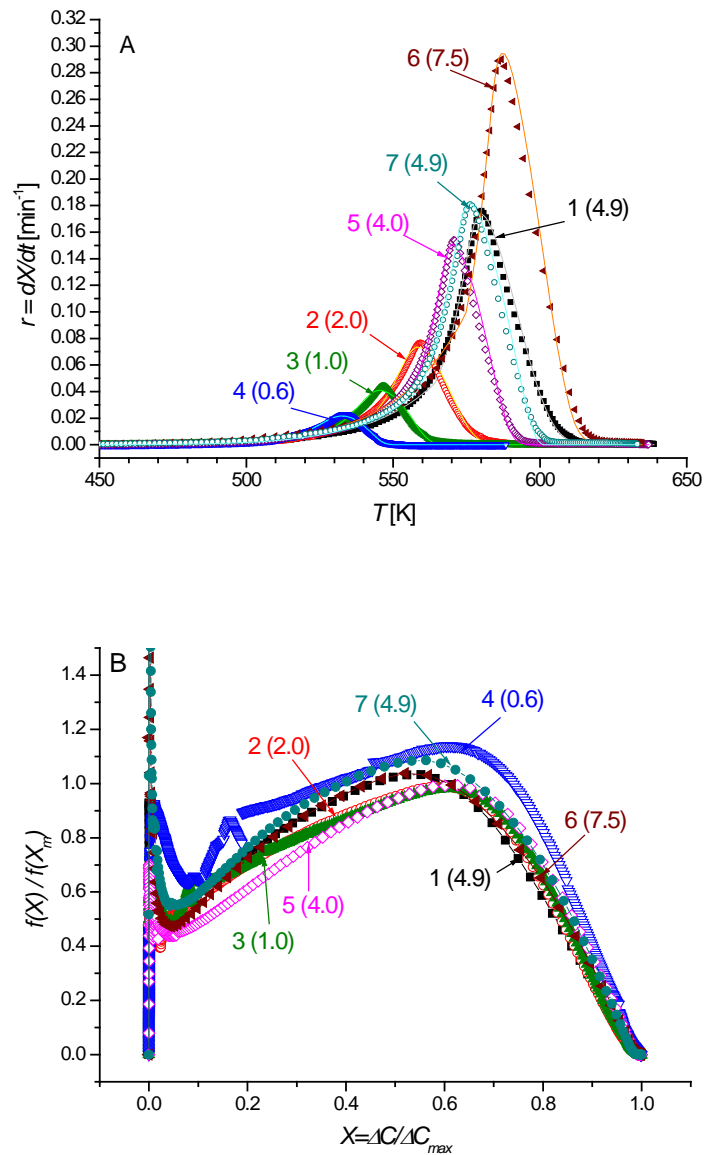
Figure S3. Experimental (points) and calculated (lines) thermal desorption spectra (A) and rate dependence functions (B) derived from the experimental TDS data for Mg + 5% C. Curve captions correspond to cycle number followed by the average heating rate [K min^{-1}] (in brackets).
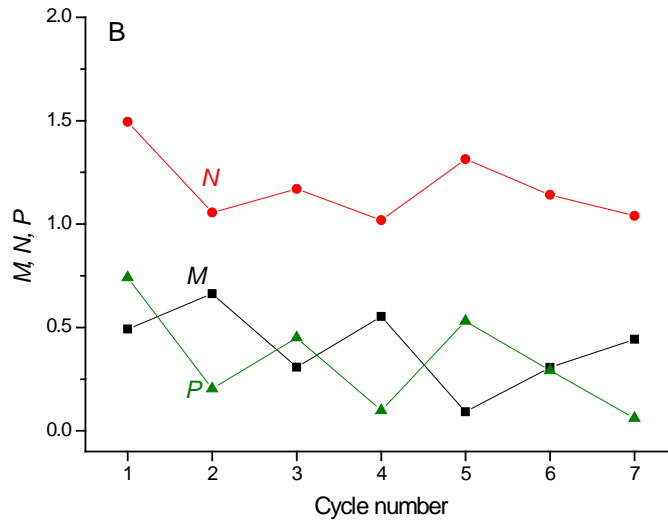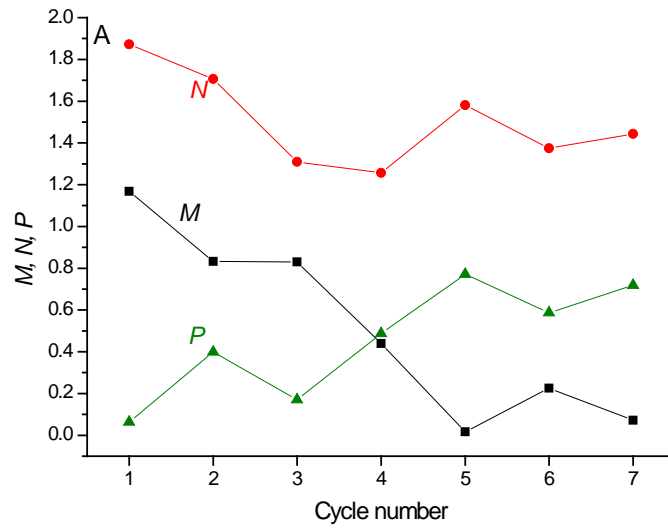
Figure S4. Dependence of fitting parameters (Eq. 4 in the main text) on the number of re-hydrogenation – dehydrogenation cycle for $Mg_{0.9}Ti_{0.1}$ (A) and $Mg_{0.9}Ti_{0.1}$ + 5% C (B).
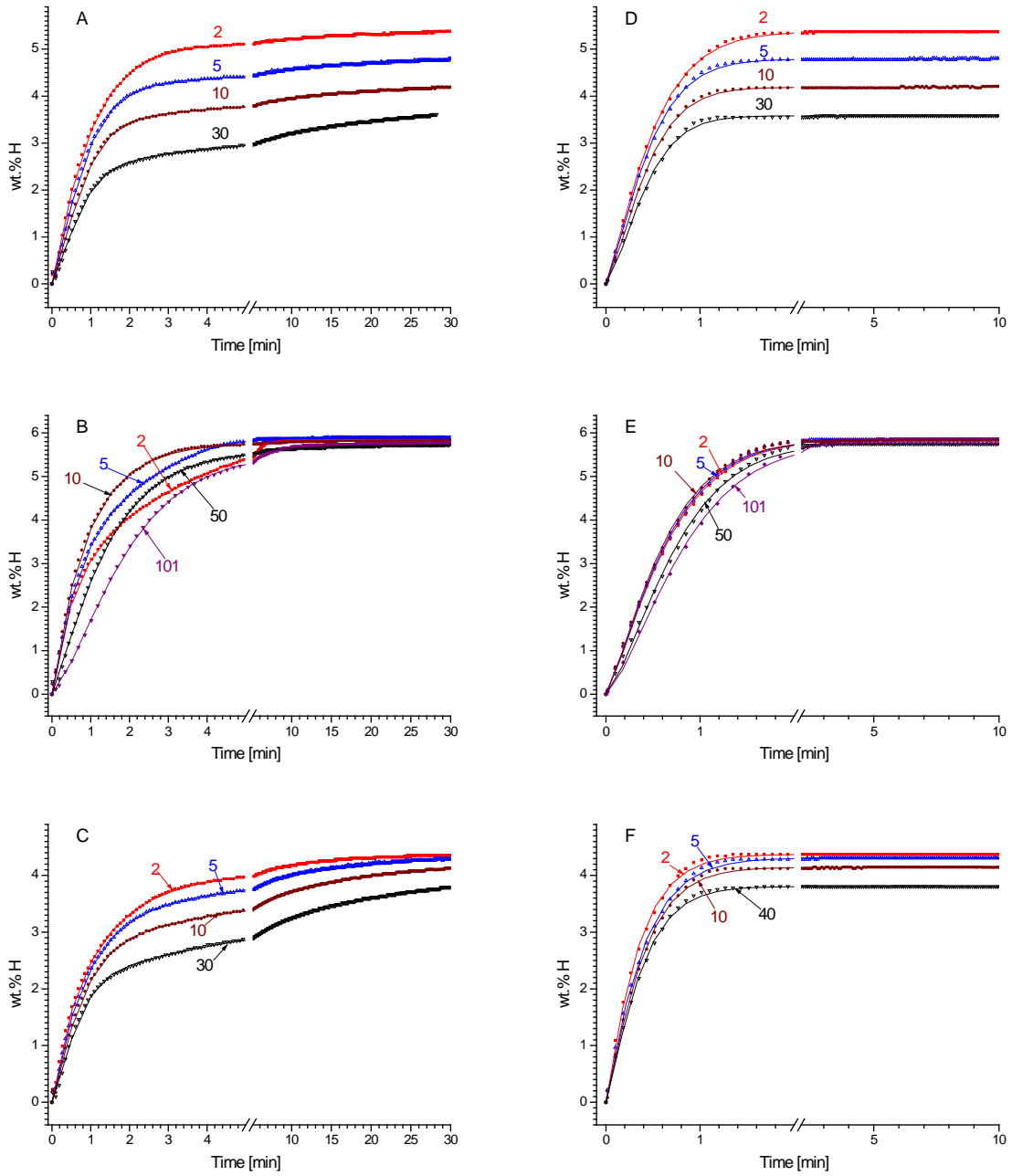
Figure S5. Hydrogen absorption (A–C) and desorption (D–F) kinetics at T=350 °C (experimental points and calculated curves) for the samples $Mg_{0.9}Ti_{0.1}$ (A, D), $Mg_{0.9}Ti_{0.1}$ + 5% C (B, E) and $Mg_{0.75}Ti_{0.25}$ (C, F). Curve labels correspond to the numbers of the absorption/desorption cycle.

Table S2. Parameters of H absorption kinetics during cycling (T=350 °C).

Sample	Cycle number (wt.% H observed)	Fitting parameters (Eq. 6) [2]								
		A_1 [wt% H]	k_1 [min^{-1}]	n_1	A_2 [wt% H]	k_2 [min^{-1}]	n_2	$N_{max}=A_1+A_2$ [wt% H]	$w_2=A_2/N_{max}$	R^2
Mg$_{0.9}$Ti$_{0.1}$	2 (5.38)	4.94(8)	1.032(4)	1.092(8)	0.5(1)	0.072(6)	0.8(2)	5.44	0.09	0.9995
	5 (4.80)	3.91(6)	1.132(7)	1.28(2)	1.01(8)	0.105(9)	0.57(5)	4.92	0.21	0.9993
	10 (4.19)	3.05(5)	1.163(8)	1.41(2)	1.24(6)	0.15(1)	0.57(3)	4.29	0.29	0.9992
	30 (3.61)	2.11(6)	1.25(1)	1.47(4)	1.77(1.9)	0.096(4)	0.61(3)	3.88	0.46	0.9990
Mg$_{0.9}$Ti$_{0.1}$ + 5%C	2 (5.85)	4.07(8)	1.35(5)	0.93(1)	1.77(8)	0.234(4)	2.13(6)	5.84	0.30	0.9997
	5 (5.88)	4.2(1)	1.45(6)	1.04(1)	1.6(1)	0.330(9)	2.2(1)	5.80	0.28	0.9997
	10 (5.83)	5.78(2)	1.066(5)	0.962(4)	0.2(1)	0.01(9)	1.3(5)	5.98	0.03	0.9994
	50 (5.73)	5.5(1)	0.678(5)	1.175(8)	0.3(1)	0.10(3)	1.0(4)	5.80	0.05	0.9996
	101 (5.78)	5.2(2)	0.50(1)	1.37(1)	0.6(2)	0.12(3)	1.6(4)	5.80	0.10	0.9997
Mg$_{0.75}$Ti$_{0.25}$	2 (4.36)	3.80(7)	1.00(2)	0.901(6)	0.58(8)	0.10(1)	1.0(1)	4.38	0.13	0.9995
	5 (4.29)	3.16(9)	1.13(1)	1.00(1)	1.2(1)	0.13(1)	0.83(7)	4.36	0.28	0.9995
	10 (4.13)	2.24(8)	1.24(1)	1.23(3)	2.02(9)	0.148(7)	0.64(3)	4.26	0.47	0.9994
	40 (3.79)	1.64(6)	1.41(1)	1.49(5)	2.39(7)	0.118(3)	0.64(2)	4.03	0.59	0.9993

Table S3. Parameters of H desorption kinetics during cycling (T=350 °C).

Sample	Cycle number (wt.% H observed)	Fitting parameters (Eq. 5)			
		N_{max} [wt% H]	k [min^{-1}]	n	R^2
Mg$_{0.9}$Ti$_{0.1}$	2 (5.37)	5.374(2)	1.899(5)	1.230(6)	0.9996
	5 (4.80)	4.790(2)	2.064(8)	1.29(1)	0.9992
	10 (4.21)	4.188(2)	2.111(9)	1.36(1)	0.9992
	30 (3.58)	3.580(3)	2.14(1)	1.43(2)	0.9984
Mg$_{0.9}$Ti$_{0.1}$ + 5%C	2 (5.85)	5.855(4)	1.419(6)	1.26(1)	0.9991
	5 (5.84)	5.852(4)	1.455(6)	1.261(9)	0.9992
	10 (5.83)	5.835(5)	1.506(5)	1.262(8)	0.9993
	50 (5.74)	5.752(5)	1.236(6)	1.39(1)	0.9987
	101 (5.76)	5.767(5)	1.104(5)	1.40(1)	0.9995
Mg$_{0.75}$Ti$_{0.25}$	2 (4.37)	4.375(2)	2.86(2)	1.09(1)	0.9987
	5 (4.31)	4.310(2)	2.53(1)	1.10(1)	0.9987
	10 (4.14)	4.145(2)	2.50(1)	1.16(1)	0.9989
	40 (3.80)	3.807(2)	2.57(1)	1.19(1)	0.9989

---

[2] Here and below the references relate to the main text of the paper
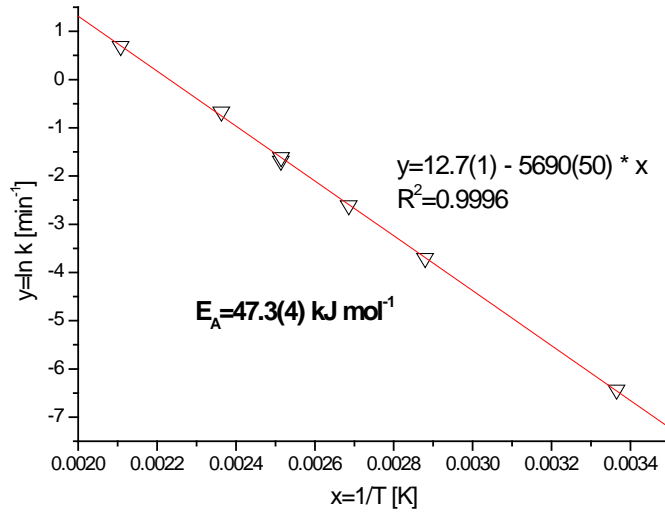
Figure S6. Arhenius plot of the rate constant for hydrogen absorption in $Mg_{0.9}Ti_{0.1}$ + 5% C calculated by the fitting of the experimental data (Figure 4A) with Eq. 5.
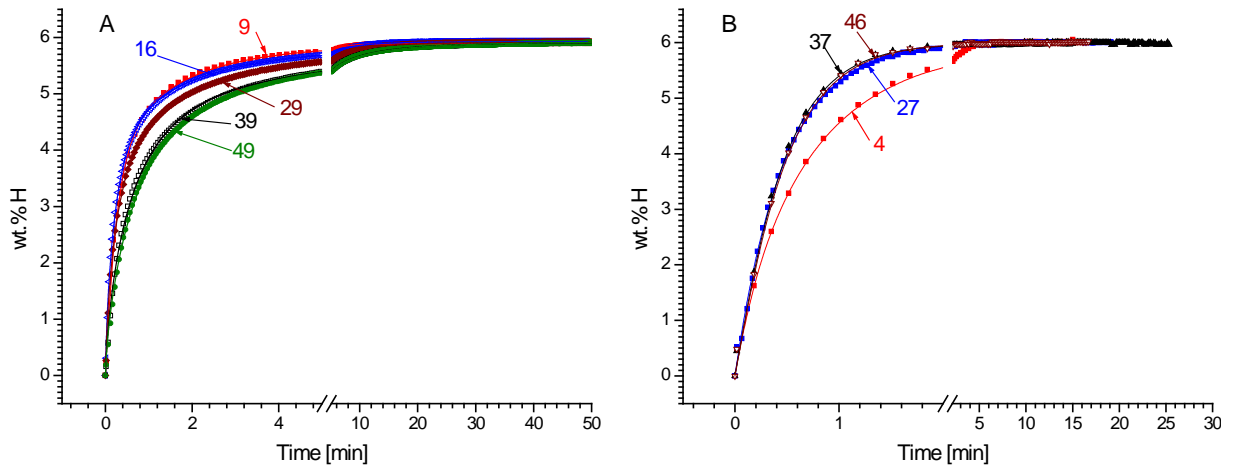
Figure S7. Hydrogen absorption kinetics for the sample $Mg_{0.9}Ti_{0.1}$ + 5% C. A – at T=200°C; B – at T=330 °C. Curve labels correspond to the number of the absorption/desorption cycle.

TableS4. Parameters of H absorption kinetics during cycling (T=100 °C).

Sample	Cycle number (wt.% H observed)	Fitting parameters (Eq. 6)								
		A_1 [wt% H]	k_1 [min⁻¹]	n_1	A_2 [wt% H]	k_2 [min⁻¹]	n_2	$N_{max}=A_1+A_2$ [wt% H]	$w_2=A_2/N_{max}$	R^2
Mg$_{0.9}$Ti$_{0.1}$	1 (5.19)	4.03(3)	0.481(4)	0.500(2)	1.35(4)	0.0041(1)	0.47(2)	5.38	0.25	0.9982
	2 (4.74)	3.21(5)	0.481(3)	0.500(4)	1.93(7)	0.00274(5)	0.40(2)	5.14	0.38	0.9974
	3 (4.50)	3.37(5)	0.318(2)	0.500(4)	1.8(2)	0.0007(1)	0.40(3)	5.17	0.35	0.9964
	5 (4.01)	2.48(3)	0.2839(8)	0.500(2)	2.02(5)	0.00182(2)	0.400(9)	4.50	0.45	0.9997
Mg$_{0.9}$Ti$_{0.1}$ + 5%C	1 (5.61)	4.22(4)	0.0396(1)	0.820(2)	1.44(5)	0.0055(2)	0.74(2)	5.66	0.25	0.9999
	2 (5.63)	4.18(7)	0.03551(5)	0.822(3)	1.45(7)	0.0086(5)	0.71(2)	5.63	0.26	0.9999
	3 (5.71)	4.33(5)	0.03801(5)	0.836(3)	1.38(5)	0.0121(5)	0.667(8)	5.71	0.24	0.9999
	5 (5.70)	4.47(7)	0.0565(1)	0.885(5)	1.22(7)	0.017(1)	0.68(1)	5.69	0.21	0.9997
	7 (5.67)	4.4(1)	0.0753(2)	0.820(6)	1.3(1)	0.016(2)	0.66(3)	5.70	0.23	0.9995
	10 (5.65)	3.69(8)	0.1067(2)	0.856(6)	1.95(8)	0.023(1)	0.67(1)	5.64	0.35	0.9996
	15 (5.65)	3.23(2)	0.1458(2)	0.912(3)	2.45(2)	0.0262(3)	0.645(3)	5.68	0.43	0.9998
	20 (5.79)	2.83(4)	0.1272(4)	0.932(7)	2.97(4)	0.0208(5)	0.578(5)	5.80	0.51	0.9996
	25 (5.35)	2.64(4)	0.1285(5)	0.949(7)	2.70(4)	0.0254(6)	0.582(5)	5.35	0.51	0.9995
	30 (5.47)	2.64(6)	0.1028(4)	0.851(8)	2.83(7)	0.0169(6)	0.598(8)	5.47	0.52	0.9996
	35 (5.64)	2.75(7)	0.0767(3)	0.763(7)	2.91(7)	0.0122(4)	0.566(8)	5.66	0.51	0.9996
	36 (5.51)	2.81(7)	0.0707(3)	0.796(7)	2.70(7)	0.0130(5)	0.571(7)	5.51	0.49	0.9994
	40 (5.49)	2.71(6)	0.0722(2)	0.825(6)	2.80(7)	0.0116(4)	0.663(9)	5.51	0.51	0.9998
	45 (5.62)	2.77(7)	0.0584(2)	0.791(7)	2.88(7)	0.0096(3)	0.607(9)	5.65	0.51	0.9997
	50 (5.63)	2.80(7)	0.0511(1)	0.802(6)	2.86(7)	0.0090(3)	0.609(8)	5.66	0.50	0.9997
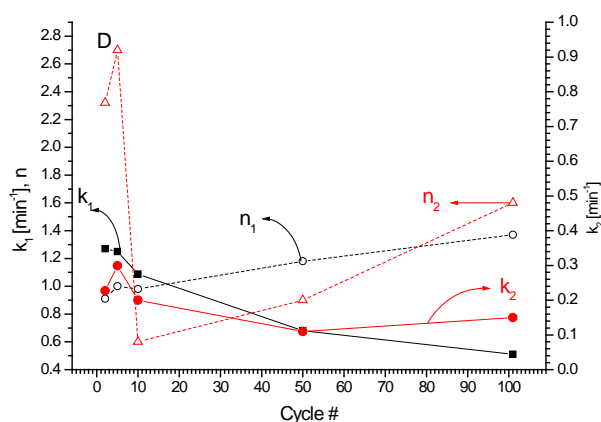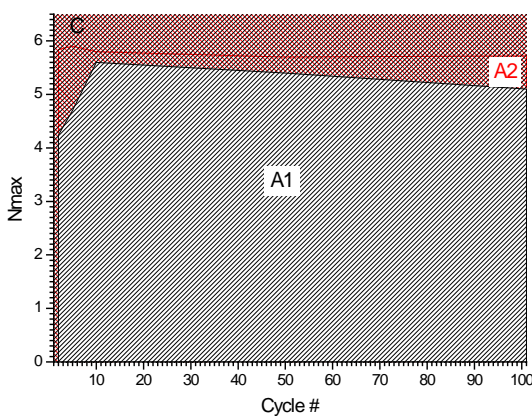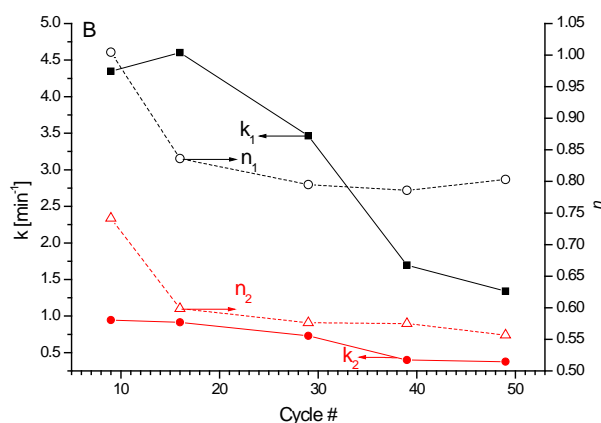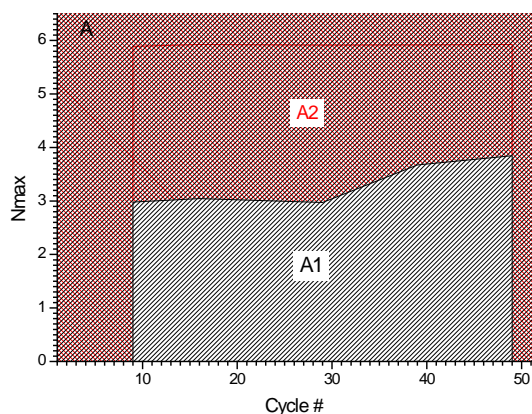
Figure S8. Change of kinetic parameters (Eq. 6) of H absorption during cycling for the sample Mg$_{0.9}$Ti$_{0.1}$ + 5% C at T=200°C (A, B) and 330°C (C, D).
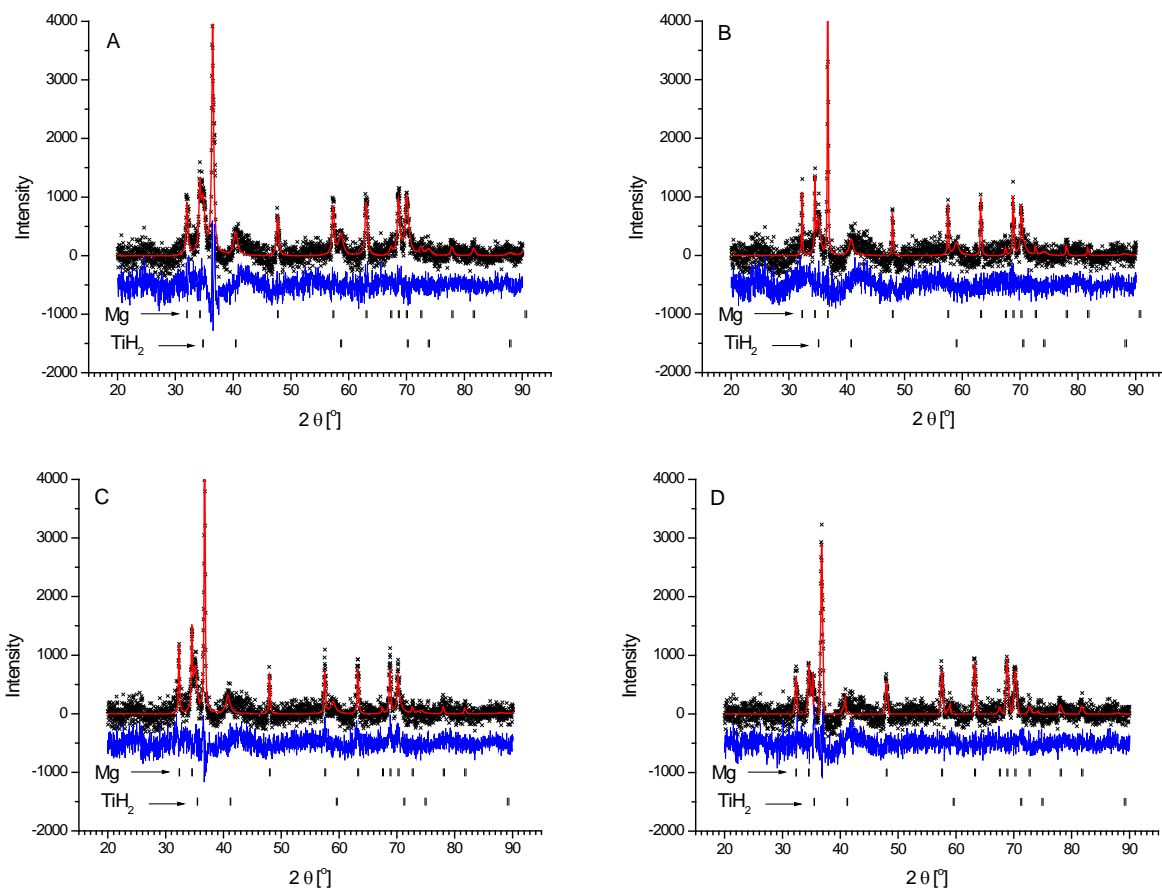
Figure S9. XRD patterns of dehydrogenated Mg$_{0.9}$Ti$_{0.1}$ (A, B) and Mg$_{0.9}$Ti$_{0.1}$ + 5% C(C, D). A, C – before cycling, B – after 30 H absorption/desorption cycles, D – after 105 absorption/desorption cycles. Background subtracted after the refinement.
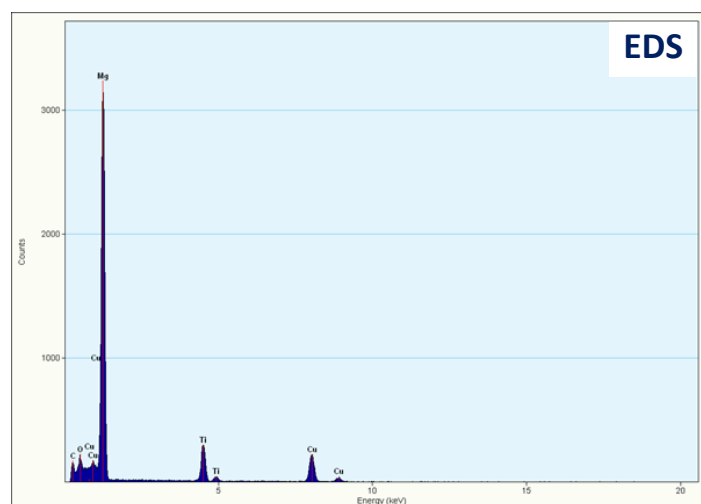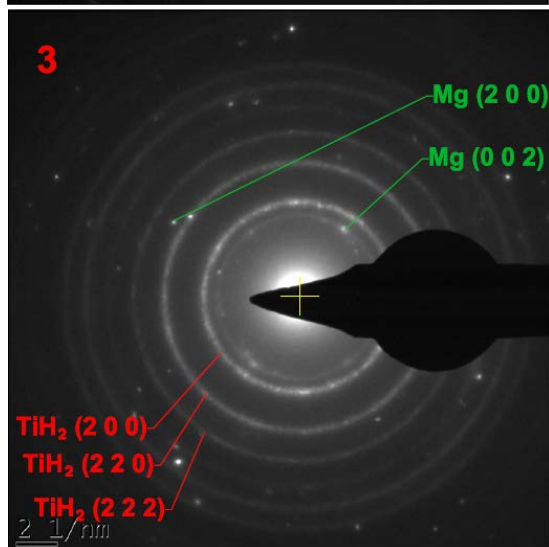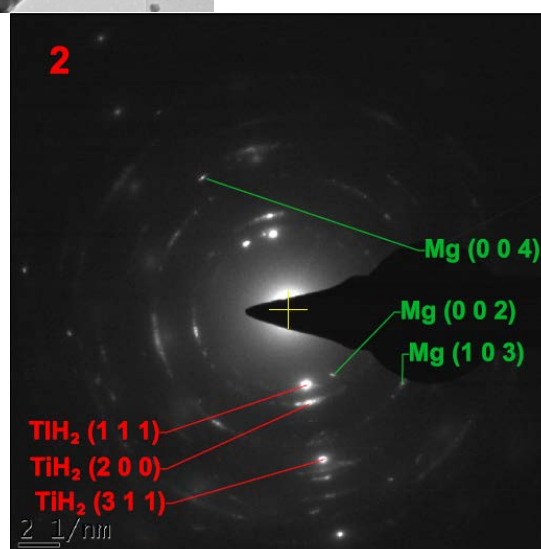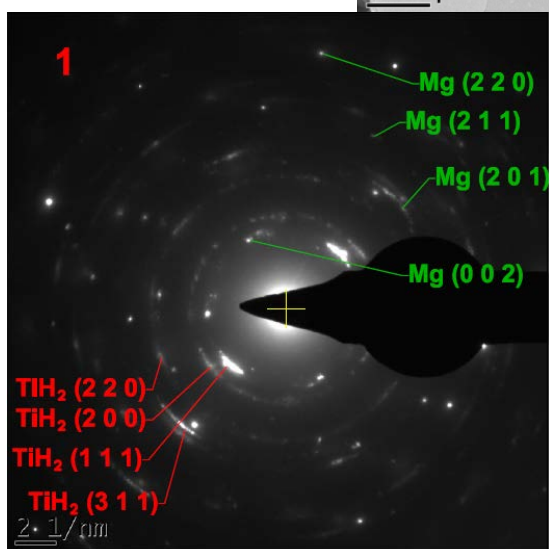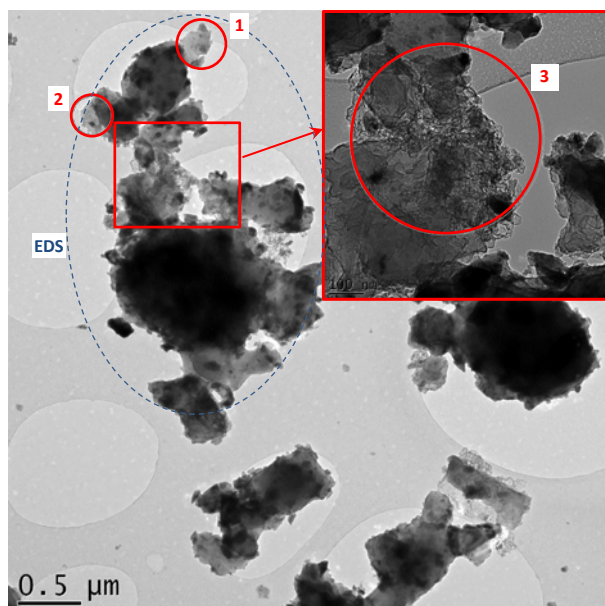
Figure S10. Top: TEM image of the sample Mg$_{0.9}$Ti$_{0.1}$. SAD patterns from areas 1, 2 and 3, and EDS[3] are shown below.

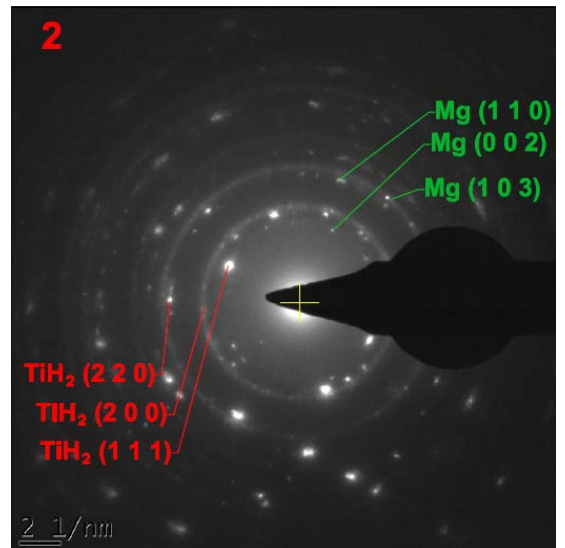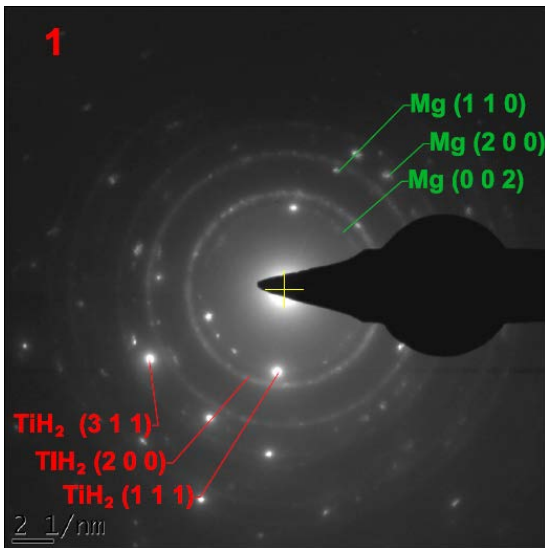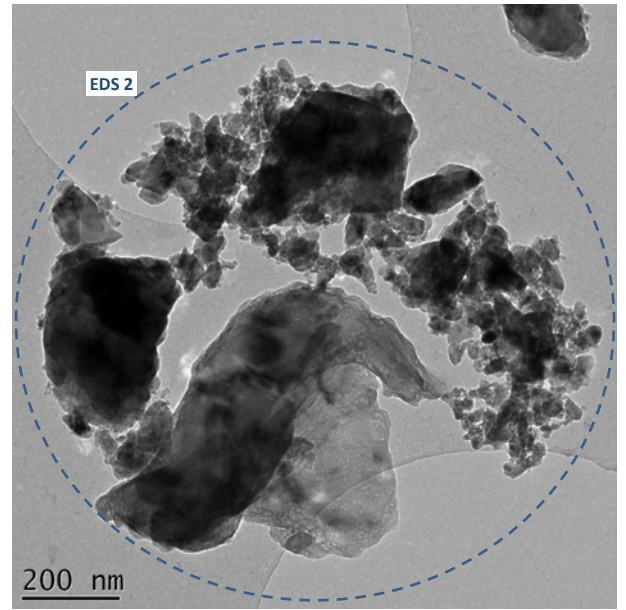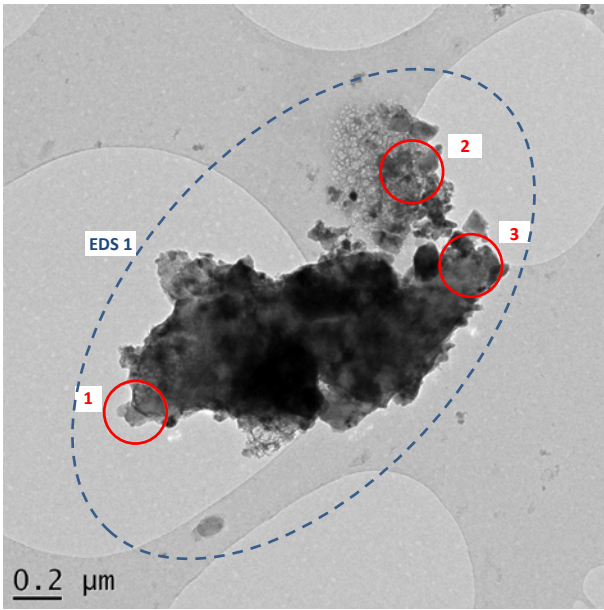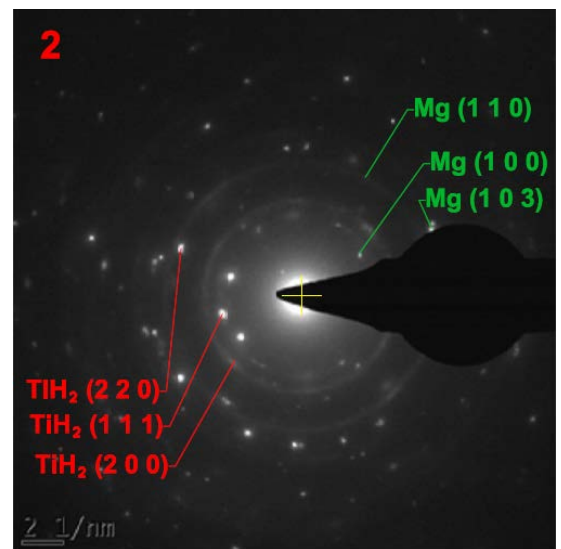[3] The observed Cu peaks in all the EDS spectra originate from the Cu grid, onto which the specimen is placed.
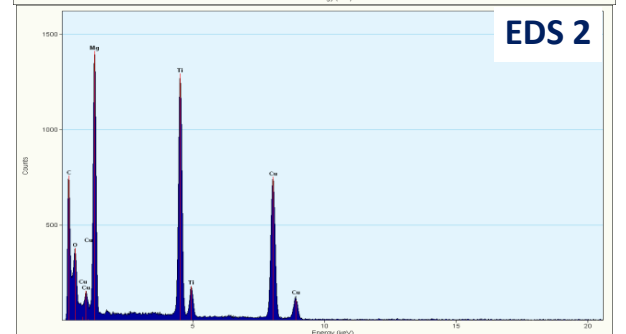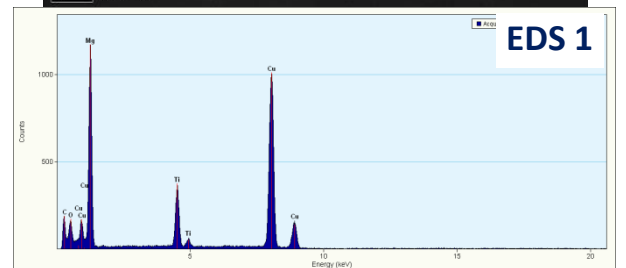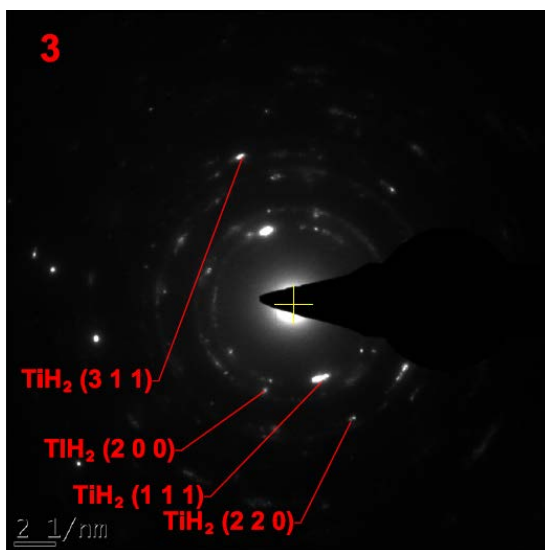
Figure S11. Top: TEM images of the sample Mg$_{0.9}$Ti$_{0.1}$ (30 cycles). SADP from areas 1, 2 and 3, and EDS are shown below.
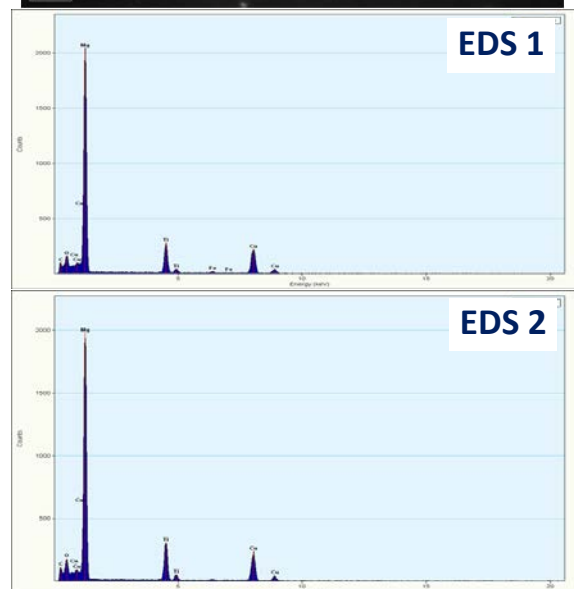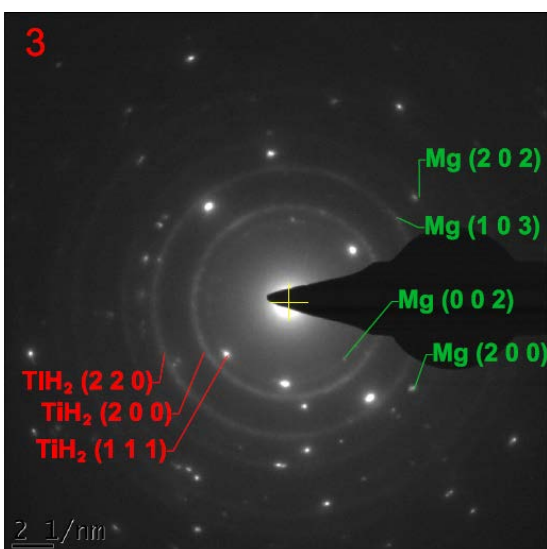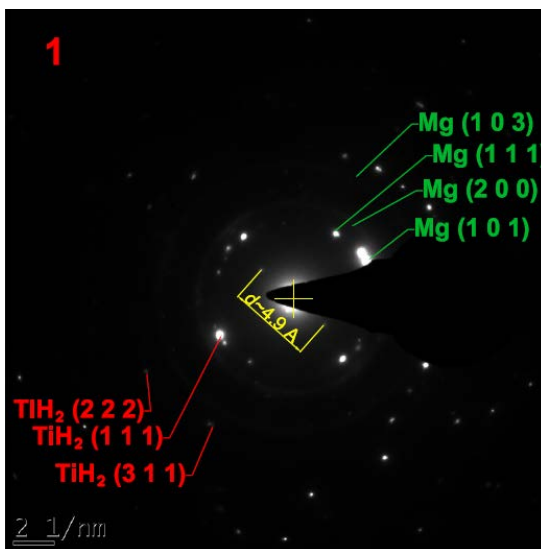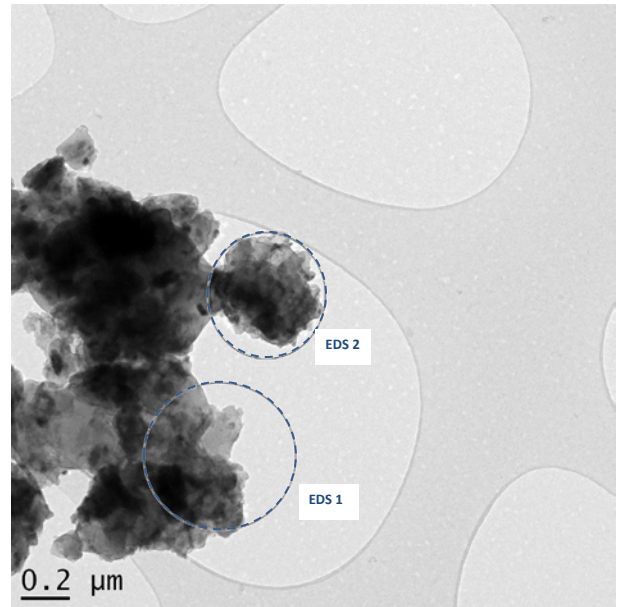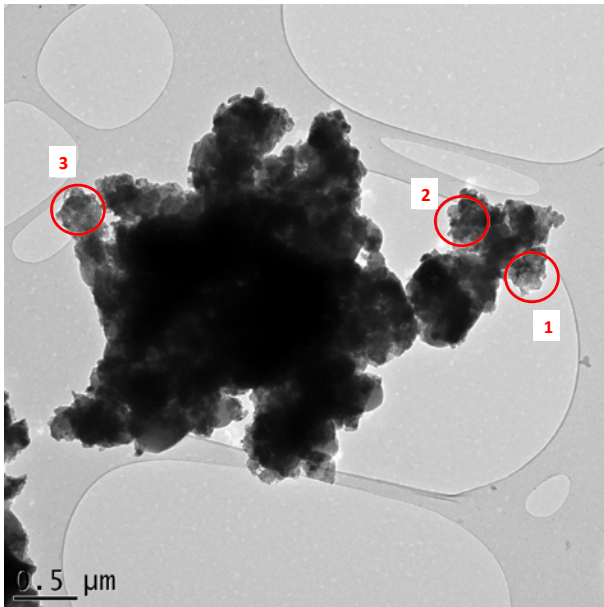
Figure S12. Top: TEM images of the sample Mg$_{0.9}$Ti$_{0.1}$ + 5% C. SADP from areas 1, 2 and 3, and EDS are shown below. Two spots with d≈4.9 Å (marked in the pattern 1) may belong to the second-order reflection from (1 0 1) plane of Mg, or (1 1 1) plane of TiH$_2$.
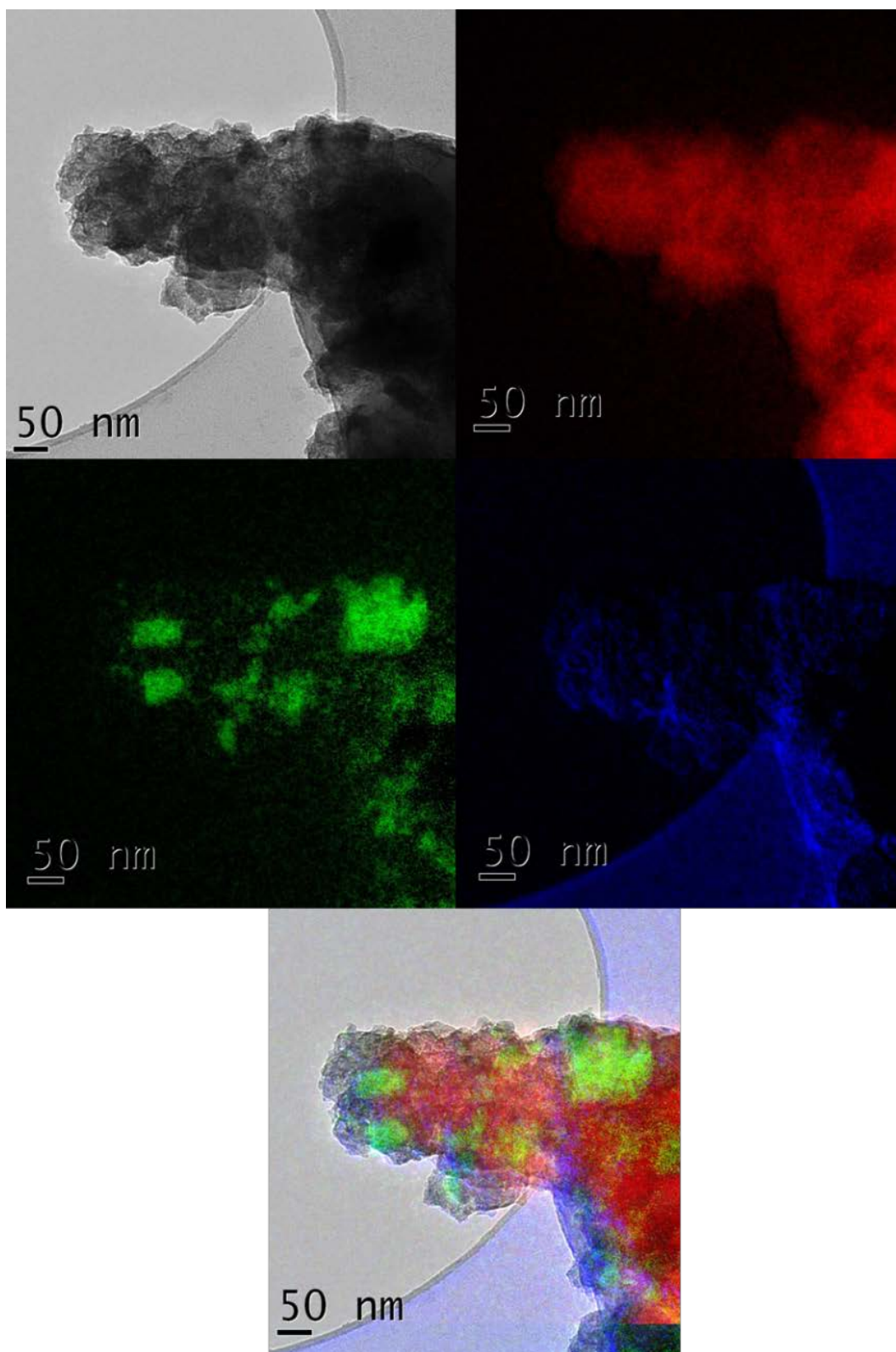
Figure S13. Top left: filtered image of $Mg_{0.9}Ti_{0.1}$ + 5% C. Top right: Mg map (red), Middle left: Ti map (green). Middle right: C map (blue). Bottom: overlayed map
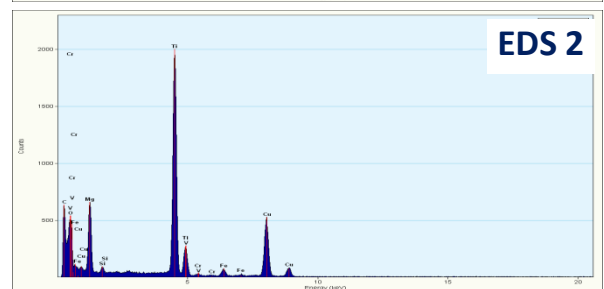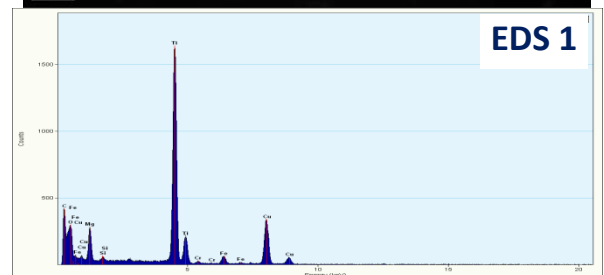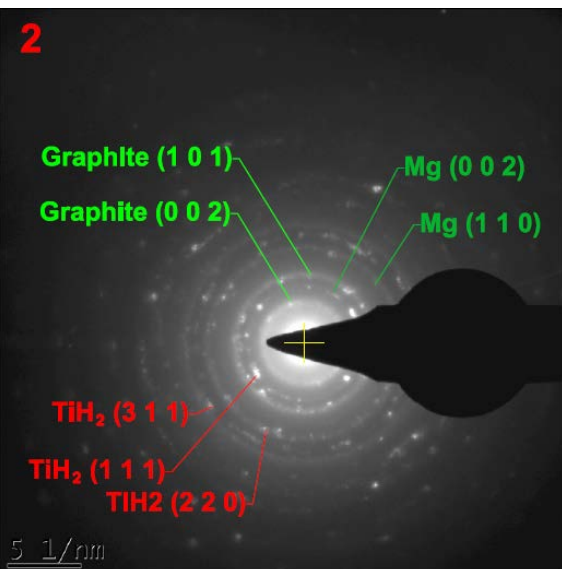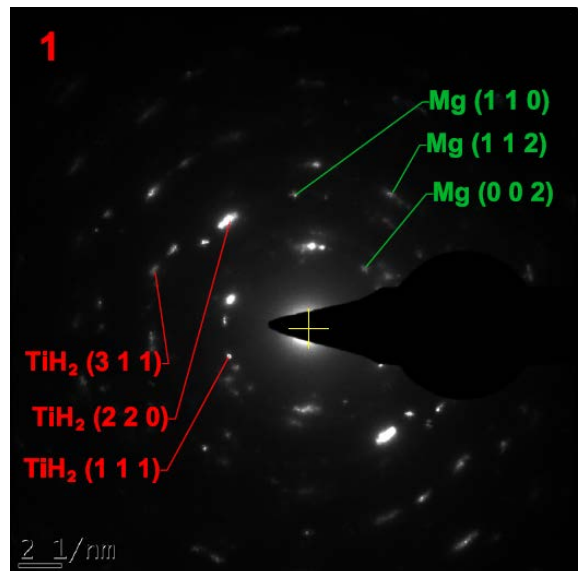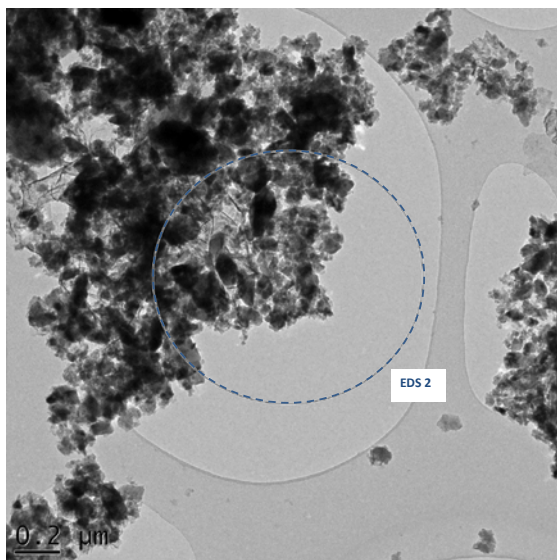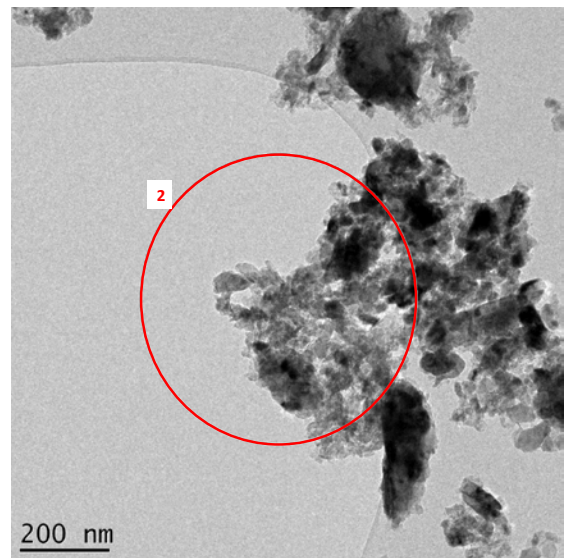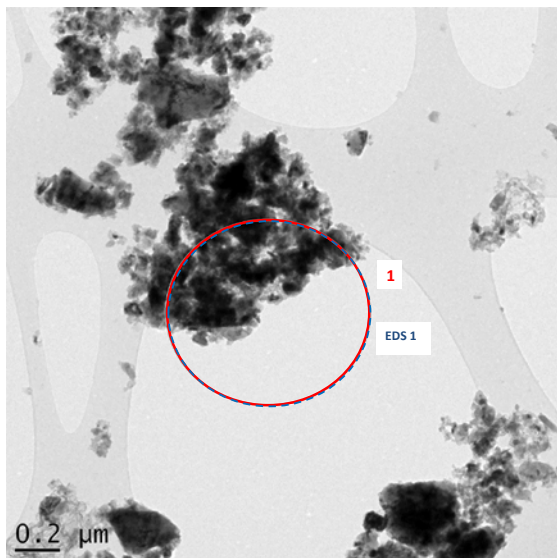
Figure S14. Top, mid-left: TEM images of the sample Mg$_{0.9}$Ti$_{0.1}$ + 5% C after 105 H absorption/desorption cycles. SADP from areas 1and 2, and EDS are shown below.
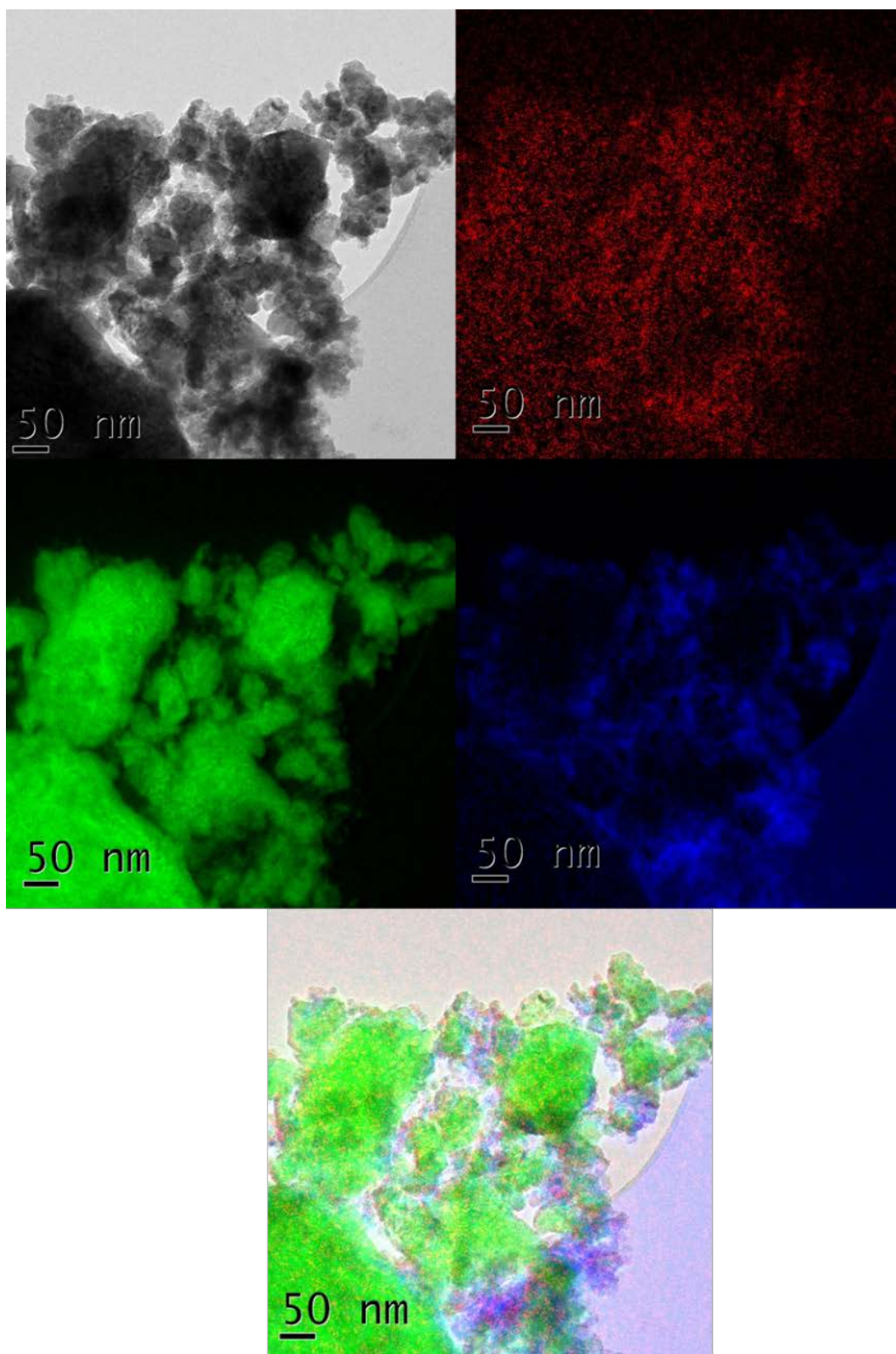
Figure S15. Top left: filtered image of $Mg_{0.9}Ti_{0.1}$ + 5%C (105 cycles). Top right: Mg map (red), Middle left: Ti map (green). Middle right: C map (blue). Bottom: overlayed map